

Observations of Herbig Ae/Be stars with Herschel/PACS. The atomic and molecular contents of their protoplanetary discs

G. Meeus, B. Montesinos, I. Mendigutía, I. Kamp, W. F. Thi, C. Eiroa, C. A. Grady, G. Mathews, G. Sandell, C. Martin-Zaïdi, et al.

▶ **To cite this version:**

G. Meeus, B. Montesinos, I. Mendigutía, I. Kamp, W. F. Thi, et al.. Observations of Herbig Ae/Be stars with Herschel/PACS. The atomic and molecular contents of their protoplanetary discs. Astronomy and Astrophysics - A&A, 2012, 544, 10.1051/0004-6361/201219225 . insu-03612413

HAL Id: insu-03612413
https://insu.hal.science/insu-03612413

Submitted on 18 Mar 2022

HAL is a multi-disciplinary open access archive for the deposit and dissemination of scientific research documents, whether they are published or not. The documents may come from teaching and research institutions in France or abroad, or from public or private research centers.

L'archive ouverte pluridisciplinaire **HAL**, est destinée au dépôt et à la diffusion de documents scientifiques de niveau recherche, publiés ou non, émanant des établissements d'enseignement et de recherche français ou étrangers, des laboratoires publics ou privés.



Distributed under a Creative Commons Attribution 4.0 International License

A&A 544, A78 (2012)
DOI: 10.1051/0004-6361/201219225
© ESO 2012

Astronomy & Astrophysics

Observations of Herbig Ae/Be stars with *Herschel*/PACS⋆

The atomic and molecular contents of their protoplanetary discs

G. Meeus[1], B. Montesinos[2], I. Mendigutía[1], I. Kamp[3], W. F. Thi[4], C. Eiroa[1], C. A. Grady[5,6,7], G. Mathews[8], G. Sandell[9], C. Martin-Zaïdi[4], S. Brittain[10], W. R. F. Dent[11], C. Howard[9], F. Ménard[4], C. Pinte[4], A. Roberge[12], B. Vandenbussche[13], and J. P. Williams[8]

[1] Universidad Autonoma de Madrid, Dpt. Fisica Teorica, Campus Cantoblanco, Spain
e-mail: gwendolyn.meeus@uam.es
[2] Dept. of Astrophysics, CAB (CSIC-INTA), ESAC Campus, PO Box 78, 28691 Villanueva de la Cañada, Spain
[3] Kapteyn Astronomical Institute, Postbus 800, 9700 AV Groningen, The Netherlands
[4] UJF-Grenoble 1/CNRS-INSU, Institut de Planétologie et d'Astrophysique (IPAG) UMR 5274, 38041 Grenoble, France
[5] Eureka Scientific, 2452 Delmer, Suite 100, Oakland CA 96002, USA
[6] ExoPlanets and Stellar Astrophysics Laboratory, Code 667, Goddard Space Flight Center, Greenbelt, MD 20771, USA
[7] Goddard Center for Astrobiology, Greenbelt, MD 20771, USA
[8] Institute for Astronomy (IfA), University of Hawaii, 2680 Woodlawn Dr., Honolulu, HI 96822, USA
[9] SOFIA-USRA, NASA Ames Research Center, Building N232, Rm 146, PO Box 1, Moffett Field, CA 94035, USA
[10] Department of Physics & Astronomy, 118 Kinard Laboratory, Clemson University, Clemson, SC 29634, USA
[11] ALMA SCO, Alonso de Córdova 3107, Vitacura, Santiago, Chile
[12] Exoplanets and Stellar Astrophysics Lab, NASA Goddard Space Flight Center, Code 667, Greenbelt, MD 20771, USA
[13] Instituut voor Sterrenkunde, Katholieke Universiteit Leuven, Celestijnenlaan 200D, 3001 Heverlee, Belgium

Received 14 March 2012 / Accepted 14 June 2012

ABSTRACT

We observed a sample of 20 representative Herbig Ae/Be stars and 5 A-type debris discs with PACS onboard *Herschel*, as part of the GAS in Protoplanetary Systems (GASPS) project. The observations were done in spectroscopic mode, and cover the far-infrared lines of [O I], [C II], CO, CH^+, H_2O, and OH. We have a [O I] 63 μm detection rate of 100% for the Herbig Ae/Be and 0% for the debris discs. The [O I] 145 μm line is only detected in 25% and CO J = 18–17 in 45% (and fewer cases for higher J transitions) of the Herbig Ae/Be stars, while for [C II] 157 μm, we often find spatially variable background contamination. We show the first detection of water in a Herbig Ae disc, HD 163296, which has a settled disc. Hydroxyl is detected as well in this disc. First seen in HD 100546, CH^+ emission is now detected for the second time in a Herbig Ae star, HD 97048. We report fluxes for each line and use the observations as line diagnostics of the gas properties. Furthermore, we look for correlations between the strength of the emission lines and either the stellar or disc parameters, such as stellar luminosity, ultraviolet and X-ray flux, accretion rate, polycyclic aromatic hydrocarbon (PAH) band strength, and flaring. We find that the stellar ultraviolet flux is the dominant excitation mechanism of [O I] 63 μm, with the highest line fluxes being found in objects with a large amount of flaring and among the largest PAH strengths. Neither the amount of accretion nor the X-ray luminosity has an influence on the line strength. We find correlations between the line flux of [O I] 63 μm and [O I] 145 μm, CO J = 18–17 and [O I] 6300 Å, and between the continuum flux at 63 μm and at 1.3 mm, while we find weak correlations between the line flux of [O I] 63 μm and the PAH luminosity, the line flux of CO J = 3–2, the continuum flux at 63 μm, the stellar effective temperature, and the Brγ luminosity. Finally, we use a combination of the [O I] 63 μm and ^{12}CO J = 2–1 line fluxes to obtain order of magnitude estimates of the disc gas masses, in agreement with the values that we find from detailed modelling of two Herbig Ae/Be stars, HD 163296 and HD 169142.

Key words. line: identification – astrochemistry – circumstellar matter – planetary systems – protoplanetary disks

1. Introduction

Circumstellar discs around young stars are the sites of planet formation (e.g. Pollack et al. 1996; Alibert et al. 2005). During the first 10 Myr, the initially gas-rich disc will evolve into first a transitional and then a debris disc, while dispersing its gas content. The understanding of this dispersal process and what favours/hinders it is a crucial part of the planet formation puzzle, as the amount of gas present in a disc is crucial to determining whether gas giant planets can still be formed. Furthermore, the disc mass controls the migration of planetary bodies of all sizes, from gas giants to metre-sized planetesimals. Three components need to be characterised well: the disc geometry, the dust, and the gas content.

The disc geometry of young intermediate-mass stars, the Herbig Ae/Be stars (HAEBEs), is constrained through multi-wavelength imaging, interferometry, and radiative transfer modelling (e.g. Benisty et al. 2010). Meeus et al. (2001) empirically divided the HAEBE discs into group I (flared) and group II (flat). A general consensus exists that discs become flatter as dust grains grow and settle towards the midplane (Dullemond & Dominik 2004). Lately, several of the group I sources have been

⋆ *Herschel* is an ESA space observatory with science instruments provided by European-led Principal Investigator consortia and with important participation from NASA.

found to have an inner opacity hole in the disc (e.g. Grady et al. 2007, 2009), possibly owing to a lack of small dust grains in the inner disc. In HD 100546, the gap may be caused by a planet (e.g. Bouwman et al. 2003; Tatulli et al. 2011).

In a study of 53 HAEBEs, 85% show a silicate emission feature at 10 μm with a variety of grain sizes and crystallinities, proving that there are *warm* small grains in these discs (Juhász et al. 2010). Polycyclic aromatic hydrocarbon (PAH) features have been detected in 70% of the sample, with a clear preference towards flared discs (Acke et al. 2010). Polycyclic aromatic hydrocarbon located in the disc atmosphere are transiently excited by ultraviolet (UV) photons and are an important heating source for the gas in the disc surface through the photo-electric effect.

The study of gas properties is difficult as, in general, emission lines are rather weak. Different gas species and transitions probe different regions in the disc: lines in the near- and mid-infrared (near-IR and mid-IR) generally trace the inner disc (<10–20 AU), while lines in the far-infrared (far-IR) and mm trace mainly the outer disc. We refer to Carmona et al. (2010) for a discussion of different gas tracers, their location in the disc, and observational characteristics. To understand the disc radial and vertical structure, it is necessary to observe several transitions of different species, as they arise under different conditions (density, temperature, and radiation field). The H_2 and CO lines are most often used, since they are the most abundant species present, with the canonical H_2 to CO number ratio in the interstellar medium being 10^4. However, the detection of H_2 in the infrared (IR) has proven to be difficult because of its weak rotational and ro-vibrational transitions – it has only been detected in 3 HAEBEs. In a survey of 15 HAEBEs with CRIRES, Carmona et al. (2011) detected ro-vibrational transitions of H_2 at 2.1218 μm in only two objects: HD 97048 and HD 100546. Earlier, Bitner et al. (2008), Carmona et al. (2008), and Martin-Zaïdi et al. (2009, 2010) searched for mid-IR pure rotational lines of H_2 at 17.035 μm in a sample of in total 20 HAEBEs; only two detections were made, in AB Aur and HD 97048. In sharp contrast, the detection of CO, although much less abundant, is easier as its rotational/ro-vibrational lines are much stronger. CO is routinely detected in HAEBEs (e.g. Thi et al. 2001; Dent et al. 2005). Lorenzetti et al. (2002) presented ISO/LWS observations of atomic and molecular lines in the far-IR for a sample of HAEBEs in which they detected the fine-structure lines of [O I] 63 μm and 145.5 μm and [C II] at 157.7 μm.

Despite the wealth of observations, it is still unclear how HAEBE discs dissipate with time. In the less massive T Tauri stars, disc dispersal is thought to be initiated by photo-evaporation, mainly due to ionising extreme-UV (EUV; $h\nu >$ 13.6 eV) photons that first create a gap in the inner disc, which is subsequently rapidly viscously accreted. In a subsequent step, the outer disc is efficiently removed through a photo-evaporative disc wind (Alexander et al. 2006). However, Gorti et al. (2009) showed that UV can rapidly disperse the outer disc, where the bulk of the disc mass is located, thus setting the disc lifetime. In addition, X-rays are thought to play an important role in these discs (e.g. Ercolano et al. 2008; Owen et al. 2012). Finally, the accretion of a planet with a mass of a few jupiters can also play an important role in the dissipation of the disc. Which mechanism ultimately dominates the dispersion process has not yet been determined.

We present ESA *Herschel* Space Observatory (Pilbratt et al. 2010) spectroscopy of 20 HAEBEs and 5 A-type debris discs, covering several transitions of abundant atoms and molecules that can be used as crucial tests of our understanding of disc physics and chemistry in the upper layers of the disc. The observations cover a significant part of the disc surface that was not accessible before. Our observations are part of the *Herschel* open time key programme (OTKP) "GAS in Protoplanetary Systems" (GASPS; P. I. Dent; see Dent et al., in prep.). With this paper, we aim to obtain a better understanding of HAEBE discs by relating several gas tracers and excitation mechanisms with stellar and disc properties. What gas species are present in a HAEBE disc and at what temperatures? What is the physical and chemical structure of the disc chemistry? What is the dominant excitation mechanism of gas in HAEBE discs?

In Sect. 2, we describe the sample and our methods to derive the stellar and disc parameters. In Sect. 3, we present the spectroscopy and the line detections. We discuss gas lines as a diagnostic tool in Sect. 4 and look for correlations between the observed line fluxes. We relate our detections and upper limits to stellar and disc parameters in Sect. 5. Finally, we round off with conclusions in Sect. 6.

2. Targets

The sample consists of 20 HAEBEs with spectral types ranging between B9.5 and F4, to which we refer as Herbig Ae (HAe) stars. We do not include the more massive Herbig Be stars which are, in general, younger and have both smaller discs and often additional remnant envelopes (e.g. Natta et al. 2000; Verhoeff et al. 2012). We also include HD 141569A, an object that completely lacks a near-IR excess for $\lambda < 4.5$ μm, an observation that we can attribute to inner disc clearing, but still has a substantial amount of primordial gas; in this paper, we refer to this a as a transitional disc. We are aware that several of our sources are also called (pre-)transitional discs in the literature, such as HD 100546 (Grady et al. 2005) and HD 135344B (Andrews et al. 2011), which are observed to have a gap in their disc, but for the purposes of this paper, we include them in the HAe sample, since they still have a substantial near-IR excess and their total IR excess is much larger than that of HD 141569A. Besides the HAe sample, we include five debris discs around A-type stars with ages between ~10 Myr and 1200 Myr for comparison, as the HAe stars are seen as their precursors. We list the main stellar parameters in Table 1. The sample is representative of the known HAe stars: there are nine objects in Meeus group I and ten in group II (to which we refer as flaring and flat discs). Furthermore, we have a good coverage of $T_{\rm eff}$, age, stellar luminosity L_*, and accretion rate. 49 Cet is the only debris disc in our sample for which gas was detected through CO observations with the JCMT (Dent et al. 2005). Hughes et al. (2008) later resolved the CO gas emission using the SMA.

For 3 stars in our sample, members of the GASPS team have performed detailed modelling of their discs with the radiative transfer code MCFOST (Pinte et al. 2006, 2009) and the thermo-chemical code ProDiMo (Woitke et al. 2009a): HD 169142 (Meeus et al. 2010), HD 100546 (Thi et al. 2011), and HD 163296 (Tilling et al. 2012).

2.1. Stellar and disc properties

To characterise the sample in a consistent way, we first attempted to determine the stellar component of the spectral energy distribution (SED). In a subsequent step, several parameters that can be important in the context of gas excitation in the disc were computed, namely, UV luminosities, IR excesses, and accretion luminosities.

Table 1. Main stellar parameters of the sample.

Star	Alternative name	Sp. type	$T_{\rm eff}$ (K)	$\log g_*$	[M/H]	Refs.	d (pc)	$L_*/L_\odot$	$A_{\rm V}$	Age (Myr)
AB Aur	HD 31293	A0 Ve	9280	4.00	*0.00*	1	139.3 ± 19.0	33.0 ± 9.2	0.25	5.0 ± 1.0
HD 31648	MWC 480	A3-5 Ve	8250	4.00	0.00	2	137.0 ± 26.2	13.7 ± 5.5	0.16	8.5 ± 2.0
HD 35187		A2 Ve	8915	*4.00*	*0.00*	3	114.2 ± 32.4	17.4 ± 10.6	0.78	9.0 ± 2.0
HD 36112	MWC 758	A5 IVe	7750	3.50	–0.08[a]	4	279.3 ± 75.0	33.7 ± 19.3	0.16	3.7 ± 2.0
					–0.14[b]	4				3.5 ± 2.0
CQ Tau	HD 36910	F3 Ve	6900	*4.35*	*0.00*	5	113.0 ± 24.0	3.4 ± 1.5	1.40	4.0 ± 2.0
HD 97048	CU Cha	A0 Ve	10000	4.00	–0.05[a]	4	158.5 ± 15.7	30.7 ± 6.1	1.15	6.5 ± 1.0
					–0.75[c]	4				4.0 ± 0.5
HD 100453		A9 Ve	7400	4.20	+0.30	6	121.5 ± 9.7	8.8 ± 1.4	0.00	>10
					–0.02[a]	4				10.0 ± 2.0
					–0.09[b]	4				9.0 ± 2.0
HD 100546		B9 Ve	10470	3.50	–0.08[a]	3, 4, 7	96.9 ± 4.0	22.7 ± 1.9	0.09	–
					–1.30[d]	4				3.8 ± 0.5
HD 104237	DX Cha	A4-5 Ve	8550	3.90	+0.16	8	114.7 ± 4.7	28.8 ± 2.4	0.16	5.5 ± 0.5
HD 135344 B	SAO 206462	F3-4 Ve	6810	4.40	+0.14[a]	10, 4	142.0 ± 27.0	8.1 ± 3.1	0.37	10.0 ± 2.0
					–0.08[b]	4				9.5 ± 2.0
HD 139614		A7 Ve	7400	4.00	–0.50	6	140 ± 42	7.6 ± 4.6	0.00	9.2 ± 2.0
					–0.19[a]	4				11.5 ± 2.0
					–0.27[b]	4				10.5 ± 2.0
HD 141569 A		B9.5 Ve	10000	4.28	–0.50	11	116.1 ± 8.1	29.6 ± 4.2	0.37	4.7 ± 0.3
HD 142527		F6 IIIe	6250	3.62	*0.00*	12	233.1 ± 56.2	33.2 ± 16.9	0.59	2.0 ± 0.5
HD 142666		A8 Ve	7500	4.30	+0.20	6	145 ± 43	13.5 ± 8.0	0.93	9.0 ± 2.0
HD 144668	HR 5999	A7 IVe	7925	*4.00*	*0.00*	13	162.9 ± 15.3	50.8 ± 9.5	0.47	2.8 ± 1.0
HD 150193	MWC 863	A2 IVe	8970	3.99	*0.00*	2	216.5 ± 76.0	48.7 ± 38.0	1.55	3.8 ± 2.0
KK Oph A		A6 Ve	8000	*4.00*	*0.00*	16	*260*	13.7	1.60	8.0 ± 2.0
KK Oph B		G5 Ve	5750	*4.50*	*0.00*	17	*260*	2.1	2.80	8.0 ± 2.0
51 Oph	HD 158643	B9.5 IIIe	10250	3.57	+0.10	2	124.4 ± 3.7	285.0 ± 17.0	0.37	0.7 ± 0.5
HD 163296	MWC 275	A1 Ve	9250	4.07	+0.20	14	118.6 ± 11.1	33.1 ± 6.2	0.47	5.5 ± 0.5
HD 169142	MWC 925	A7-8 Ve	7500	4.00	–0.50	15	145 ± 43	9.4 ± 5.6	0.00	7.7 ± 2.0
49 Cet	HD 9672	A4 V	9500	4.30	+0.10	2	59.4 ± 1.0	21.0 ± 0.7	0.22	$8.9^{+6.1}_{-2.4}$, 61^{+119}_{-46}
HD 32297		A0 V	9520	*4.15*	*0.00*	18	112.4 ± 10.8	10.9 ± 2.1	0.62	–
HR 1998	HD 38678, ζ Lep	A2 IV-V	8500	4.27	–0.76	9, 19	21.6 ± 0.1	14.0 ± 0.1	0.00	1250 ± 250
HR 4796 A	HD 109573 A	A0 Ve	9750	4.32	*0.00*	9	72.8 ± 1.8	23.4 ± 1.1	0.00	10.0 ± 2.0
HD 158352	HR 6507	A7 V	7500	3.85	*0.00*	9	59.6 ± 0.9	17.7 ± 0.6	0.00	1000 ± 200

Notes. Quantities in *italics* are assigned. [(a)] These metallicities are weighted averages of all the elemental abundances listed in Tables 2–4 of Acke & Waelkens (2004); see Appendix A of Montesinos et al. (2009) for details. [(b–d)] Metallicities assumed to be in the same proportion as the species [Fe I]/([Si II])/[Fe II], respectively (see Table 3 of Acke & Waelkens 2004).

References. (1) Woitke et al. (GASPS) (in prep.), (2) Montesinos et al. (2009), (3) Manoj et al. (2006), (4) Acke & Waelkens (2004), (5) Testi et al. (2003), (6) Guimarães et al. (2006), (7) Levenhagen et al. (2006), (8) Fumel & Böhm (2012), (9) Allende-Prieto et al. (1999), (10) Müller et al. (2011), (11) Merín et al. (2004), (12) Verhoeff et al. (2011), (13) van Boekel et al. (2005), (14) Tilling et al. (GASPS) (2012), (15) Meeus et al. (GASPS) (2010), (16) Herbig (2005), (17) Carmona et al. (2007), (18) Torres et al. (2006), (19) Gray (2006). Distances are from the revised parallaxes by van Leeuwen (2007), except for HD 135344 B (Müller et al. 2011) and HD 139614, HD 142666, and HD 169142 (van Boekel et al. 2005).

We compiled a set of literature and catalogue stellar parameters (effective temperatures, gravities, and metallicities), and critically selected what we considered to be the most accurate. Multi-wavelength photometry from different sources and UV spectra obtained by the International Ultraviolet Explorer[1] were used to construct the SED of the star-plus-disc systems. A specific model photosphere for each star was extracted, or computed by interpolation, from the grid of PHOENIX/GAIA models (Brott & Hauschildt 2005). A Rayleigh-Jeans extension up to mm wavelengths was applied to the original models. The model photosphere was reddened with several values of $E(B-V)$ ($R_V = 3.1$) and normalised to the flux at V (0.55 μm), until the closest fit to the optical photometry was achieved. In some cases, the photospheric model fits the UV spectrum fairly well, implying that there is only a stellar photospheric contribution in that spectral range, whereas in other cases an excess, attributed to accretion processes, was apparent.

The photospheric, IR, and UV fluxes (required to estimate the stellar luminosity, $L_{\rm IR}/L_*$, and $L_{\rm UV}/L_\odot$) were all computed from the *dereddened* data or model. The photospheric flux was estimated by integrating the model photosphere; the IR flux was computed by fitting a spline to the observed data set, integrating from the shortest wavelength λ_0 where the fit started to differ from the photospheric model up to 200 μm; the UV flux between 1150–2430 Å was then used to compute $L_{\rm UV}$. Accretion rates were estimated from the observed photometric excesses in the Balmer discontinuity. These were modelled assuming a magnetospheric accretion geometry, following the procedure of Mendigutía et al. (2011b). Upper limits to the accretion rates are provided for most stars, given that the Balmer excesses are negligible.

[1] http://sdc.cab.inta-csic.es/ines/

Table 2. Derived properties of the sample.

Star	Disc group	L_{IR}/L_*	$L_{UV}/L_\odot$	$\log L_{acc}/L_\odot$
AB Aur	I	0.76	4.63	<0.55
HD 31648	II	0.46	0.75	<0.19
HD 35187	II	0.12	2.23	1.13
HD 36112	I	0.66	1.32	<−0.81
CQ Tau	II	1.01	0.19–0.3	<−1.16
HD 97048	I	0.39	7.69	<0.95
HD 100453	I	0.62	0.29	<−0.91
HD 100546	I	0.56	7.22	1.62
HD 104237	II	0.32	1.54	0.87
HD 135344 B	I	0.56	0.11[a]	−0.22
HD 139614	I	0.39	0.39	<−1.12
HD 141569 A	II/TO	0.009	6.83	<0.70
HD 142527	I	0.98	0.15[a]	<−1.04
HD 142666	II	0.33	0.37–0.68	0.85
HD 144668	II	0.51	1.55–2.94	<0.23
HD 150193	II	0.48	8.53	1.32
KK Oph A+B	II	2.01	2.35	1.70
51 Oph	II	0.03	71.32	<0.37
HD 163296	II	0.29	3.21–5.58	−0.04
HD 169142	I	0.42	0.45	<0.05
49 Cet	Debris	6.0×10^{-4}	2.96	<−0.11
HD 32297	Debris	0.003	1.91[a]	–
HR 1998	Debris	6.6×10^{-5}	1.25	–
HR 4796 A	Debris	0.003	5.59	–
HD 158352	Debris	1.6×10^{-4}	0.64	–

Notes. Disc group classification from Meeus et al. (2001) and Acke et al. (2010). For the derivation of L_{IR}/L_*, $L_{UV}/L_\odot$, and $\log L_{acc}/L_\odot$, see the description in Sect. 2.1. Disc groups I and II refer to Meeus et al. (2001) classification, "TO" stands for "transition object". [(a)] Ultraviolet fluxes measured on the model photosphere (no UV observations available).

In Table 1, we give some of the basic parameters of the stars, namely identifications, spectral types, effective temperatures, gravities, metallicities, and the corresponding references (Cols. 1–7), distances (Col. 8), and two parameters derived from those and the SEDs, namely stellar luminosities and ages (Cols. 9 and 10). In Table 2, we list either the disc groups according to Meeus et al. (2001) or the evolutionary status of the stars, fractional IR luminosities, UV luminosities, and accretion luminosities (Cols. 2–5). Stars with two values of $L_{UV}/L_\odot$ in Col. 4 have two different emissivity levels in IUE spectra obtained at different epochs; the numbers corresponding to both the low and high states are given.

The age estimations were done by placing the values of $\log T_{eff} - \log L_*/L_\odot$ for each star on a Hertzsprung-Russel (HR) diagram containing tracks and isochrones computed for its particular metallicity. For some stars, this parameter is unknown, thus a solar abundance was assumed, which introduced an uncertainty that was difficult to estimate. Metallicity is an important parameter to take into account when determining ages using this procedure since the position of a set of tracks and isochrones in the HR diagram changes substantially with metallicity. The evolutionary tracks and isochrones for a scaled solar mixture from the Yonsei-Yale group (Yi et al. 2001) – Y^2 in their notation – were used in this work. From the Y^2 set, the isochrones with $Z = 0.02$ (solar) were used for stars with measured metallicities [M/H] between −0.10 and +0.10 and for the stars for which no abundance determinations were available. The remaining metallicities were treated with the isochrones in the grid whose value of Z is closer to $0.02 \times 10^{[M/H]}$.

There is one star, HD 32297, for which a determination of the age was impossible; its position falls below the main sequence in a $Z = 0.02$ HR diagram, therefore, it is quite likely that this star has subsolar abundance. We note that the evolutionary stage of 49 Cet is interesting and was studied in detail in Montesinos et al. (2009). Two ages for this star, corresponding to pre-main sequence and main sequence isochrones, are listed in Table 1.

2.1.1. KK Oph

Special attention had to be paid to KK Oph. This object is a close binary separated by 1.61 arcsec (300 AU at our adopted distance; see discussion below and Leinert et al. 1997), the hot component (A) being a HAe star and the cool component (B) a T Tauri star, both of which are actively accreting (Herbig, 2005, and references therein). The SED shows an IR excess from ∼1 μm onwards. All the available photometry corresponds to both components, therefore it is not straighforward to estimate parameters for each star from these data alone. In addition, the system is highly variable (Hillenbrand et al. 1992; Herbst & Shevchenko 1999; Eiroa et al. 2001; Oudmaijer et al. 2001), adding further complications to the analysis.

Herbig (2005) determined an spectral type A6 V for KK Oph A, and Carmona et al. (2007) – who only studied the secondary component – found a spectral type G5 V for KK Oph B. In both cases, the authors used high specral-resolution spectroscopy, which allowed them to separate the spectra of each component. Effective temperatures of 8000 K and 5750 K were assigned to the stars according to their spectral types. To estimate luminosities from the available photometry, we followed the approach of Carmona et al. (2007), where each star is assumed to be affected by a different extinction, adopting $A_V = 1.6$ and 2.8 mag for components A and B, respectively. We analysed the set of optical and near-IR photometry provided by Hillenbrand et al. (1992), and assumed that the contribution to the flux at U and B from the cool component was negligible. The distance to this system is uncertain, with published values of 170–200 pc. We find these distances too low to obtain values for the luminosities of the stars that agree with their spectral type and luminosity class; a lower limit of ∼260 pc provides sensible results and was adopted in this work, as the most reliable distance we could derive with the available data set.

3. *Herschel*/PACS spectroscopy

We obtained PACS (Poglitsch et al. 2010) spectroscopy in both line and range modes (PacsLineSpec, 1669 s and PacsRangeSpec, 5150 s). The observation identifiers (obsids) can be found in Table A.1.1 of Appendix A. At a later stage, we obtained deeper range scans to confirm tentative detections by doubling the integration time for 7 sources. All the observations were carried out in ChopNod mode, to remove the emission of the telescope and background. The instrument PACS is an IFU with 25 spaxels, 9.″4 on each side. Owing to the characteristics of the PSF at 60 μm, only ∼70% of a point source flux falls in the central spaxel, with a decrease towards longer wavelengths, down to 45% at 180 μm.

The spectroscopic data were reduced with the official release version 8.0.1 of the *Herschel* interactive processing environment (HIPE; Ott 2010), using standard tasks provided in HIPE. These include bad pixel flagging, chop on/off subtraction, spectral response function division, and rebinning with oversample =2 and upsample =1 corresponding to the native resolution of the instrument, spectral flatfielding, and finally averaging of the two nod

Table 3. Ranges and lines targeted with the PACS spectrometer.

Set	Observed range λ (μm)	Species	Transition	Wavelength (μm)
A	62.68–63.68	[O I]	$^3P_1 \rightarrow {}^3P_2$	63.184
		o-H_2O	$8_{18} \rightarrow 7_{07}$	63.324
	188.77–190.30	DCO^+	J = 22–21	189.570
B	71.90 –73.05	o-H_2O	$7_{07} \rightarrow 6_{16}$	71.946
		CH^+	J = 5–4	72.14
		CO	J = 36–35	72.843
	144.0–146.1	p-H_2O	$4_{13} \rightarrow 3_{22}$	144.518
		CO	J = 18–17	144.784
		[O I]	$^3P_0 \rightarrow {}^3P_1$	145.525
C	78.55–79.45	o-H_2O	$4_{23} \rightarrow 3_{12}$	78.741
		OH	1/2 - - 3/2	79.11
		OH	1/2 +- 3/2	79.18
		CO	J = 33–32	79.360
	157.1–158.9	[C II]	$^2P_{3/2} \rightarrow {}^2P_{1/2}$	157.741
		p-H_2O	$3_{31} \rightarrow 4_{04}$	158.309
D	89.45–90.50	p-H_2O	$3_{22} \rightarrow 2_{11}$	89.988
		CH+	J = 4–3	90.02
		CO	J = 29–28	90.163
	178.9–181.0	o-H_2O	$2_{12} \rightarrow 1_{01}$	179.527
		CH^+	J = 2–1	179.610
		o-H_2O	$2_{21} \rightarrow 2_{12}$	180.488

positions. To ensure the highest quality of signal and to prevent introducing additional noise, we only extracted the central spaxel and corrected for the flux loss with an aperture correction provided by the PACS instrument team ("pointSourceLossCorrection.py"). This is only possible when the source is well-centred. If that was not the case (e.g. for HD 142666), several spaxels needed to be taken into consideration to gather all of the target emission.

The main lines targeted are the fine-structure lines of [O I]and [C II] and the molecular lines of CO, OH, CH^+, and H_2O. In total, we observed eight spectral regions; the details of the transitions can be found in Table 3. The spectral resolution varies between 3400 (shortest wavelengths) and 1100 (longest wavelengths), which are equivalent to ~88 km s^{-1} at 60 μm, and 177 km s^{-1} at 190 μm. In our sample, we did not resolve the emission lines as our objects do not have such high velocity components. The line flux sensitivity is of the order of 10^{-18} W/m^2. The lines were identified by manual inspection of automated Gaussian fits at the expected line position, taking the instrumental resolution as the expected full width at half maximum (FWHM) of the line. We extracted the fluxes of the detected lines using a Gaussian fit to the emission lines with a first-order polynomial to the continuum. We used the root mean square (rms) of the continuum (excluding the line) to derive a 1σ error for the line by integrating a Gaussian with height equal to the continuum rms and width equal to the instrumental FWHM. This approach is necessary as HIPE currently does not deliver errors for the spectra. In case of a non-detection, we give a 3σ upper limit, which was also calculated from the continuum rms. The absolute flux calibration error given by the PACS instrument team is currently <15%. The measured line fluxes – in the cases of detection – or their upper limits are listed in Tables 4 and 5. Several atomic and molecular lines were observed, as described in the following paragraphs.

3.1. Oxygen fine-structure lines

The third most abundant element in the interstellar medium is oxygen. Its fine-structure line at 63.2 μm is by far the strongest

Table 4. Atomic line strengths in units of 10^{-18} W/m^2 with 1σ continuum rms between brackets in the case of a detection or 3σ upper limits.

Star λ (μm)	[O I] 63.18	[O I] 145.53	[C II] 157.75
AB Aur	851.2 (21.5)	44.6 (14.7)	51.0 (8.3)
HD 31648	94.9 (3.5)	<7.8	<9.7
HD 35187	32.8 (4.8)	<4.6	<5.9
HD 36112	37.3 (2.4)	<6.3	<9.6
CQ Tau	47.9 (4.0)	<3.8	<11.3
HD 97048	1592.5 (4.3)	65.6 (2.6)	106.8 (6.3)
HD 100453	61.6 (7.5)	<6.1	<15.4
HD 100546	6043.4 (13.4)	194.7 (9.9)	203.8 (8.6)
HD 104237	79.1 (3.5)	<5.9	<7.6
HD 135344B	47.9 (5.8)	<4.6	<6.4
HD 139614	44.5 (6.1)	<4.7	<8.3
HD 141569A	245.3 (4.8)	24.9 (1.4)	11.4 (2.1)
HD 142527	52.3 (3.8)	<11.6	<28.7
HD 142666	18.9 (3.1)	<4.7	<9.0
HD 144668	140.2 (4.3)	<5.8	<5.4
HD 150193	24.6 (2.8)	<6.6	<5.3
KK Oph	172.8 (5.0)	6.2 (1.3)	9.2 (1.2)
51 Oph	53.3 (2.5)	<5.1	<6.8
HD 163296	208.4 (4.2)	<4.0	ABS[a]
HD 169142	91.5 (4.4)	<3.6	<8.0
49 Cet	<10.0	<6.3	<9.1
HD 32297	<7.4	<4.2	<7.1
HR 1998	<7.0	<5.1	<6.6
HR 4796A	<6.3	<3.8	<5.4
HD 158352	<8.2	n.a.	<3.8

Notes. For HD 158352, not all settings were observed, therefore we write "n.a." (not available) when the spectrum is lacking. [(a)] An absorption feature is observed in the spectrum, that is caused by the subtraction of stronger emission in the chop-off position.

Table 5. CO line strengths in units of 10^{-18} W/m^2, 1σ continuum rms between brackets in the case of a detection or, in the case of a non-detection, 3σ upper limits.

Star λ (μm)	CO J36-35 72.85	CO J33-32 79.36	CO J29-28 90.16	CO J18-17 144.78
AB Aur	<37.9	<33.4	31.0 (4.3)	26.6 (8.8)
HD 31648	<9.6	<16.3	<9.6	6.9 (2.3)
HD 35187	<21.0	<28.9	<8.4	<5.5
HD 36112	<30.2	<17.6	<17.7	6.6 (1.1)
CQ Tau	<15.4	<25.4	<9.9	5.9 (1.5)
HD 97048	<21.3	<16.6	15.3: (6.0)	28.5 (2.6)
HD 100453	<13.9	<19.5	<9.6	<8.3
HD 100546	<28.7	<38.8	49.3 (16.1)	58.0 (3.3)
HD 104237	<19.6	<16.1	<9.8	<5.6
HD 135344B	<13.0	<21.7	<8.5	<8.4
HD 139614	<16.4	<19.9	<9.0	<6.9
HD 141569A	<12.3	<10.6	<6.6	<3.4
HD 142527	<30.9	<23.7	<12.4	<9.8
HD 142666	<16.3	<18.8	<12.6	<6.2
HD 144668	<11.9	<12.1	<8.2	5.6 (1.3)
HD 150193	<14.8	<13.1	<7.2	<6.2
KK Oph	<6.5	<9.4	<7.7	6.9 (1.3)
51 Oph	<9.0	<12.4	<6.6	<4.0
HD 163296	<8.0	<10.7	<7.9	11.6 (1.5)
HD 169142	<10.0	<10.9	<10.0	5.1: (1.7)
49 Cet	<13.6	<18.6	<9.8	<6.7
HD 32297	<11.4	<16.9	<9.7	<4.3
HR 1998	<12.6	<13.5	<6.6	<4.8
HR 4796A	<12.8	<17.1	<7.6	<4.1
HD 158352	n.a.	<9.2	n.a.	n.a.

Notes. With ":", we indicate that the feature is between 2σ and 3σ. For HD 158352, not all settings were observed, therefore we write "n.a." (not available) when the spectrum is lacking.

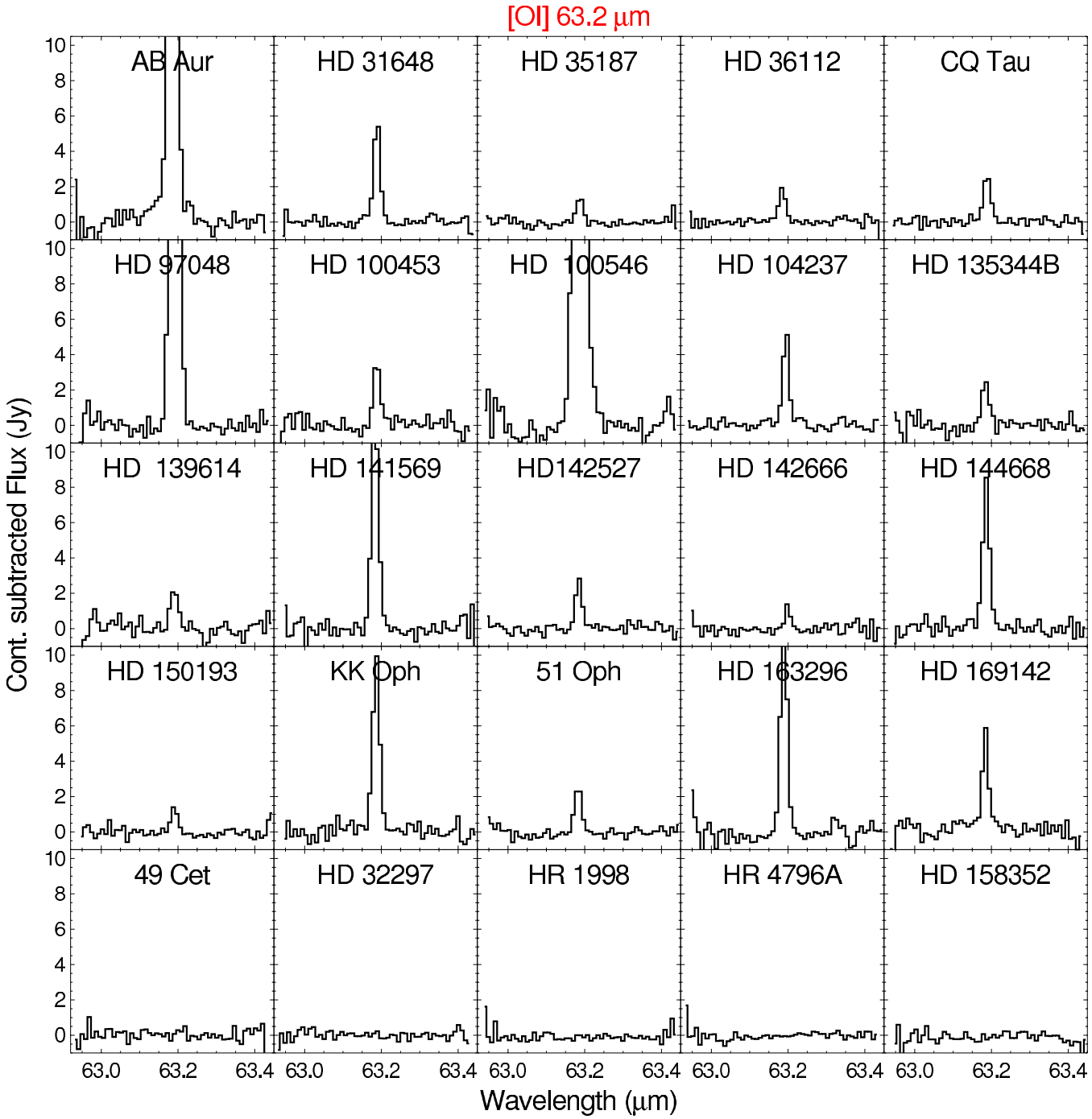


Fig. 1. The [O I] 63 μm lines for the entire sample. The line is seen in emission in all the HAEBEs, while it is absent in the more evolved debris-disc objects 49 Cet, HD 32297, HR 1998, HR 4796A, and HD 158352 (*bottom row*).

line observed in our spectra (see Table 4). It is detected in all HAEBEs, and absent in the debris discs. For five of our objects, the line flux is higher than 200×10^{-18} W/m^2, while our faintest detection is 20×10^{-18} W/m^2. The other fine-structure line [O I] 145 μm is also one of the strongest lines in our spectra, although it is only detected in five objects (25% of the HAEBEs). In Figs. 1 and 2, we show the spectra centred on [O I] 63 μm and [O I] 145 μm for the whole sample.

3.2. Carbon fine-structure line

When detected, the [C II] 157.7 μm line can be strong – more than 100×10^{-18} W/m^2. However, it is only seen in six objects (30% of the HAEBEs; see Fig. 3) – these are the same objects for which [O I] 145 μm was also detected (see Table 4), apart from HD 36112. The low detection rate for [C II] is surprising, given the high detection rate (83%) in ISO/LWS spectra reported by Lorenzetti et al. (2002). This can be attributed to a difference in aperture: 80 arcsec for LWS versus 9 arcsec for PACS. Moreover, we note that the line can also be present in the off-source chop positions (in a spatially variable amount), contaminating our spectra. In two cases, the dominating emission is present in all on- and off-source spaxels, so that our chop-off subtracted spectra even show the feature in absorption as the chop-off position spectra contain stronger emission (HD 142527 and HD 163296, see Fig. 3). The interpretation of

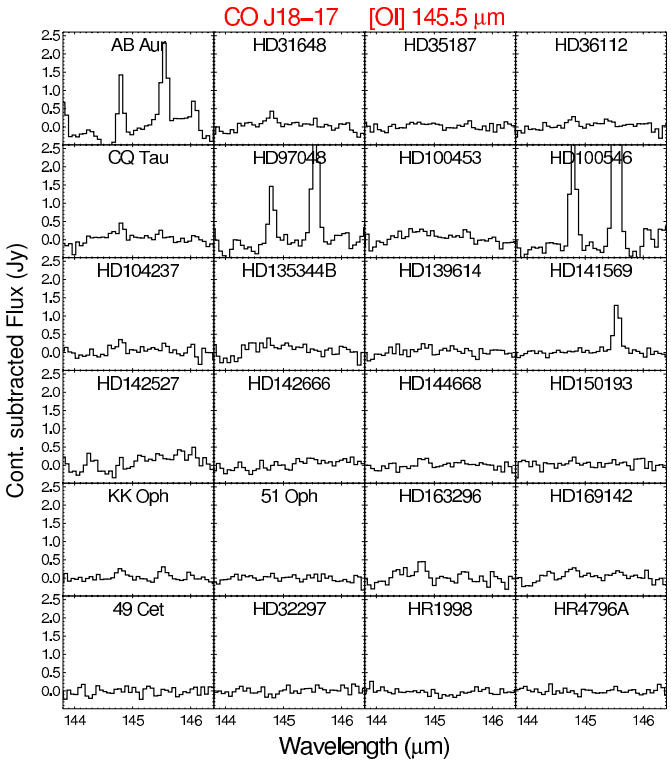


Fig. 2. The settings around 145 μm. The lines of CO J = 18–17 at 144.8 μm and [O I] 145 μm are only clearly detected in three objects, while [O I] 145 μm is clearly detected in HD 141569A.

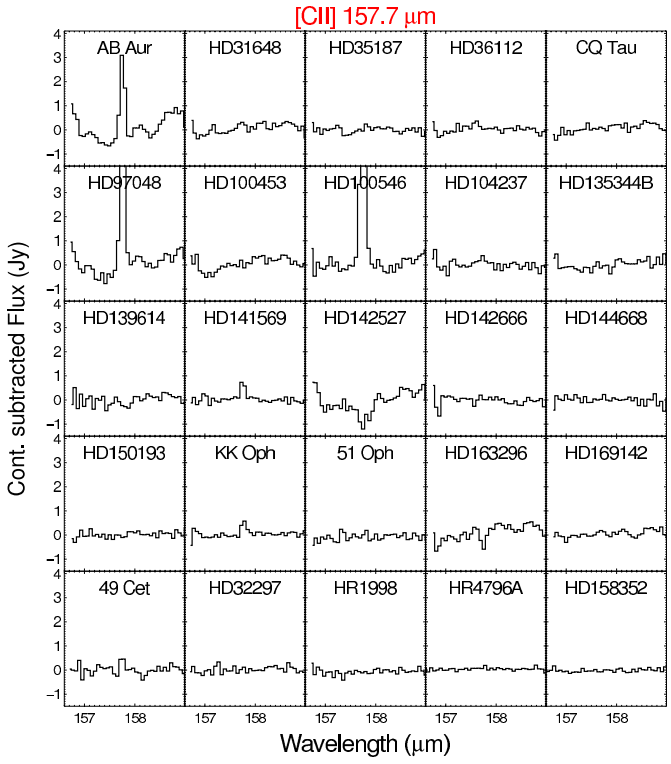


Fig. 3. The [C II] line at 157.7 μm. The line is only clearly detected in three objects, more weakly in three others, and appears in absorption in HD 142527 and HD 163296, owing to the subtraction of the chop-off spectrum containing stronger emission lines.

the [C II] emission line is complex. Besides originating in the disc, it could also form in the remaining envelope, or simply

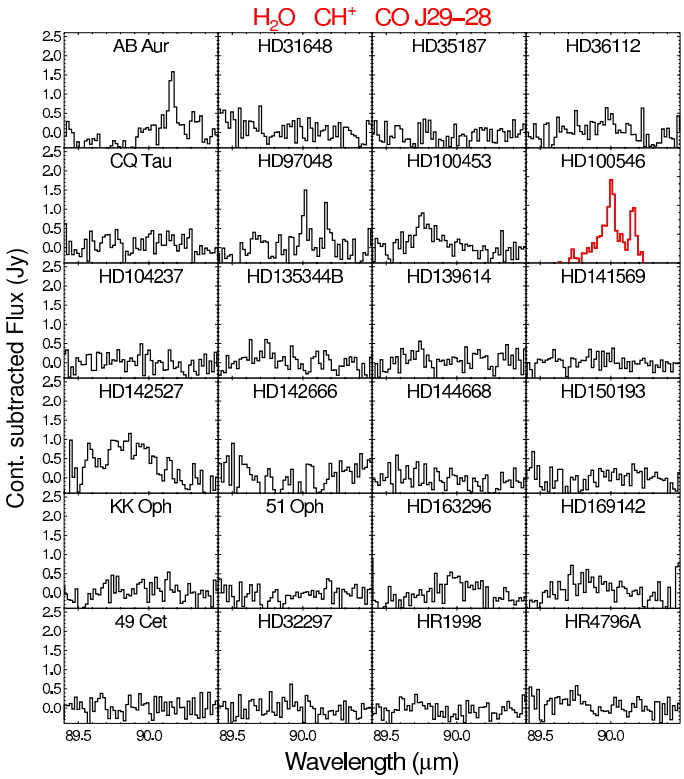


Fig. 4. The spectra around 90 μm, covering p-H_2O at 89.988, CH^+ at 90.02 and CO at 90.163 μm. The only sources with clearly detected lines are AB Aur (CO), HD 97048 and HD 100546 (CH^+ and CO). HD 100546 is scaled by a factor of 1/4, to ensure that the emission lines fit in the plot window.

in cloud material along the line of sight. A detailed analysis of background [C II] emission is beyond the scope of this paper, but a dedicated study is underway (Pantin et al., in prep.).

3.3. Carbon monoxide

In our PACS ranges, we cover four transitions of the CO molecule: J = 36–35 (72.85 μm), J = 33–32 (79.36 μm), J = 29–28 (90.16 μm), and J = 18–17 (144.78 μm). These are all mid to higher J transitions, with E_{up} between ~950 K and 3700 K. The highest J transitions in our settings (J = 36–35 and J = 33–32) are not detected in any star of our sample. In Fig. 4, we show the region around 90 μm, covering the CO J = 29–28 transition. This CO line is only clearly seen in AB Aur and HD 100546, with a tentative detection for HD 97048. For the lowest J observable (18–17, at 144.78 μm), we see many more detections in our spectra (see Fig. 2): it is detected in nine objects, and there is one tentative detection, that for HD 169142. The strongest CO lines are observed in AB Aur, HD 97048 and HD 100546. The star HD 141569A is the only one for which we have a clear (more than 5σ) detection of [O I] 145 μm, but no detection of CO at 144.78 μm, showing that both species trace different excitation conditions and chemistry (atomic versus molecular). We discuss this further in Sect. 4.3.

3.4. Hydroxyl

With our settings, we only cover the OH doublet at 79.11/79.18 μm. In Fig. 5, we can see evidence for the doublet in

Table 6. Molecular line strengths of H_2O, hydroxyl, and CH^+ for the sources with at least one detection in these lines.

Star	o-H_2O	o-H_2O	CH^+	o-H_2O	OH	OH	CH^+/p-H_2O	CH^+/o-H_2O	o-H_2O
λ (μm)	63.32	71.946	72.14	78.74	79.11	79.18	90.00	179.52	180.42
E_{up} (K)	1071.0	843.5	–	432.2	–	–	296.8	114.4	194.1
AB Aur	<29.8	<19.0	<36.7	<26.5	24.6: (7.9)	<24.8	<18.4	<13.5	<8.2
HD 31648	9.8: (2.2)	<12.4	<21.6	<17.7	<9.9	<10.3	<9.1	<7.5	<5.9
HD 97048	<16.4	<16.8	<18.6	<18.2	<17.0	<18.9	17.4 (4.9)	<18.3	<13.8
HD 100546	<25.9	<50.9	127.5 (17.0)	<57.0	<41.9	<42.1	116.0 (16.1)	30.5 (4.8)	<17.1
HD 163296	14.2: (4.4)	16.5 (5.3)	<19.9	10.2: (4.1)	11.4 (3.4)	<9.1	4.7: (1.9)	<10.4	<6.2

Notes. Line flux in units of 10^{-18} W/m^2, 1σ continuum rms between brackets in the case of a detection, or, in the case of a non-detection, 3σ upper limits. With ":", we indicate that the feature is between 2σ and 3σ. At 90 μm and 179.5 μm, there is a possible blend of CH^+ and H_2O. For the water lines, we also give the upper energy level in K.

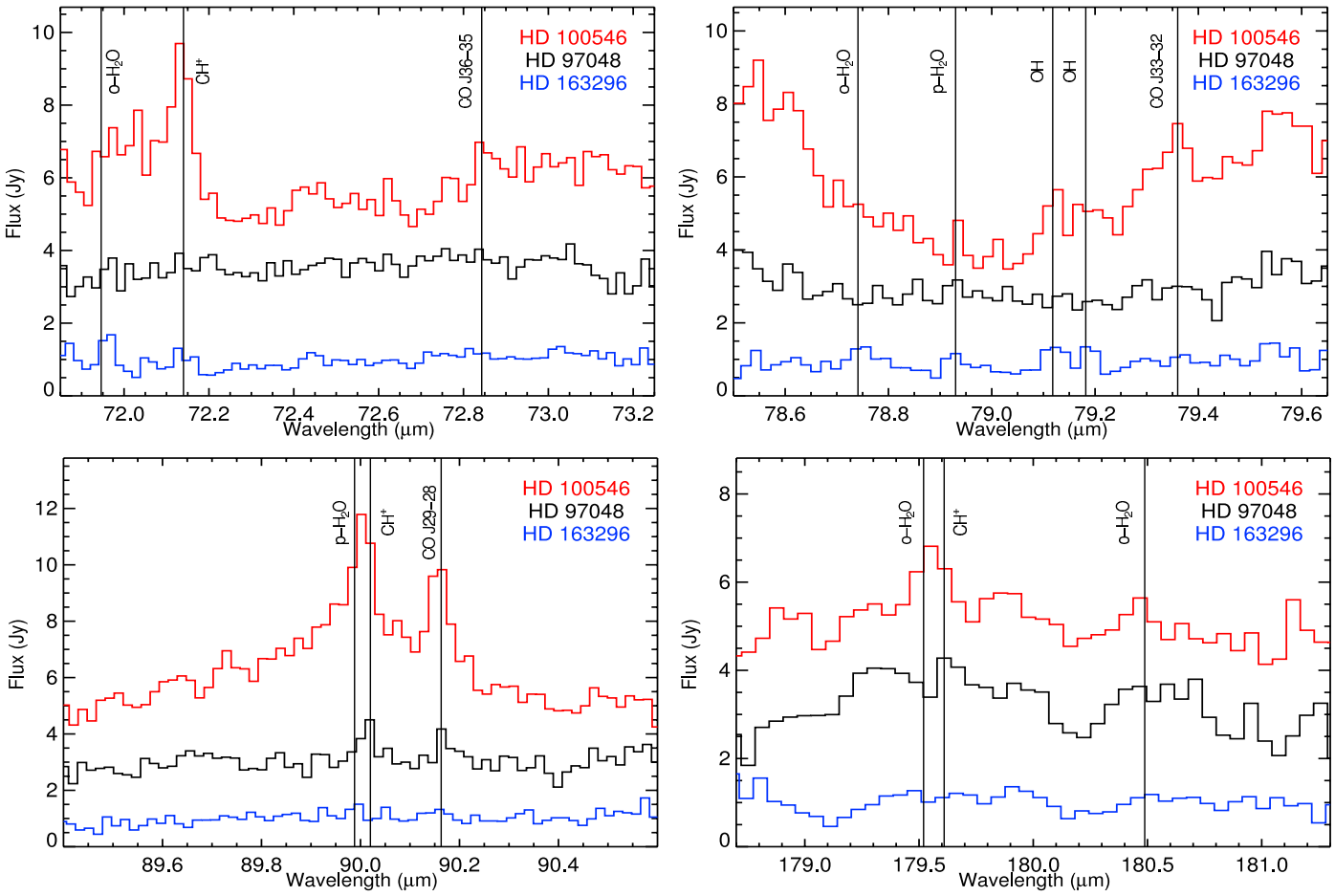


Fig. 5. Comparison of HD 100546 (*top* spectrum), HD 97048 (*middle*), and HD 163296 (*bottom*) at 72.6 and 79.0, 90.0, and 180.0 μm. We indicate the positions of the lines of CO, CH^+, OH, and H_2O.

HD 100546 and HD 163296; however, the only 3σ detections (of one line of this doublet) were made for AB Aur and HD 163296 (see Table 6). Sturm et al. (2010) detected several OH lines at far-IR wavelengths (53–200 μm) in the SED-mode PACS spectra of HD 100546.

3.5. Water

The only star in our sample with convincing evidence of water is HD 163296. The measured line fluxes are listed in Table 6. While the feature at 63.32 μm is seen in HD 163296 with 3σ confidence, we list it as a tentative detection given the spurious absorption feature next to it (in HD 31648, a potential feature of water at 63.32 μm is redshifted by 0.009 μm, so we also consider it a tentative detection). In our deeper range scans at 71.946 μm and 78.74 μm, we also see evidence for water in HD 163296 (see Fig. 5). The features are close to 3σ, although that we do see emission lines at the positions where water lines are predicted to be present strengthens the detection of water in HD 163296. The analysis of the water in HD 163296 is presented in a separate paper (Meeus et al., in prep.).

In two other objects, HD 97048 and HD 100546, we do see several emission lines at the position of water. In Fig. 4, we show the region around 90 micron, where the transition of para-H_2O can appear. However, when we zoom in on these stars in the

regions where other water lines are expected to be present, we get a different picture; in Fig. 5, we show the spectra covering water lines. At 90.00 μm (see Fig. 5), we see an emission peak for both stars, which could be the para-H_2O line (at 89.988 μm), but it is also a blend with CH^+ at 90.02 μm. At other positions of water that are not blended with CH^+, we do not see any emission line at 71.948, 78.741, 78.93, and 180.488 μm.

To summarise, the only times that we detected an emission feature at the position of a water line in these two objects, was in a blend with CH^+. We can conclude that there are no H_2O emission lines detected in these two objects at the sensitivity of our observations. We therefore, do not confirm the detection of water in HD 100546 reported by Sturm et al. (2010), as these authors also found in a later improved reduction of their original data (Sturm, priv. comm.).

3.6. CH^+

Thi et al. (2011) reported the first detection of CH^+ in a Herbig Ae/Be disc, HD 100546. We detected the feature of CH^+ in both HD 97048 and HD 100546 at 90.00 μm. For HD 100546, we have detections of two more lines, at 72.14 μm and 179.61 μm. The features at 90.0 μm and 179.6 μm are also at the position of water features, but given the lack of other water features, they can be attributed to CH^+.

4. Gas lines as tracers of the conditions in the disc

The far-IR lines observed with PACS form in different regions of the disc. The exact locations vary with geometry, i.e. flaring, inner holes, gaps, but we discuss here for simplicity the general case of a continuous flaring disc around a HAe star.

The [C II] line depends strongly on the irradiation of the star, especially UV photons shortward of 1200 Å (Pinte et al. 2010; Kamp et al. 2011). The emission originates foremost in the upper tenuous layers of the disc (low critical density) where UV photons can penetrate. The [O I] 63 μm and [O I] 145 μm lines form deeper in the disc where the atomic oxygen abundance is still high. Most of their emission comes from regions at 10–100 AU as the temperatures beyond 100 AU are generally too low to excite these lines (Kamp et al. 2010). The high-excitation water lines ($E_{up} \geq 400$ K) form mostly in the surface layers of the hot water reservoir inside the snow line (15 AU for an effective temperature of 10 500 K, moving inwards for cooler stars while keeping the disc structure constant). The low-excitation lines ($E_{up} \leq 200$ K) form in a thin layer beyond the snow line where water can be photo-desorbed from the icy grains into the gas phase (Cernicharo et al. 2009; Woitke et al. 2009b). The exception is the 89.988 μm water line with an upper level energy of ~300 K, which forms across the snow line (for TW Hya, a T Tauri disc – Kamp et al., in prep.). Bruderer et al. (2012) modelled the CO ladder in HD 100546. They found that the high J lines of CO can only be reproduced by a warm atmosphere in which T_{gas} is much higher than T_{dust}. The low J lines of CO (observed in the mm) trace the outer disc (at several 100 AU radial distance), while the mid to high J lines observed in the far-IR originate at distance of several tens of AU. The highest J lines of CO form mostly in the very inner disc, which is typically within a few AU, or at the rim of transition discs.

The fundamental ro-vibrational CO band ($\Delta v = 1$) at 4.7 μm band, which traces the terrestrial planet-forming region is routinely observed in HAEBEs (e.g. Brittain et al. 2007). The bands are rotationally excited up to high J (>30), with T_{rot} between 900 K and 2500 K (van der Plas et al. 2012). If the gas is not in local thermal equilibrium (LTE), then the vibrational temperature, T_{vib}, can depart from T_{rot}, when UV fluorescence causes the presence of super-thermal level populations. This is observed in several UV-bright HAEBEs where $T_{vib} > 5000$ K: HD 97048 and HD 100546 have $T_{vib} > 6000$ K, while their $T_{rot} \sim 1000$ K (Brittain et al. 2007; van der Plas et al. 2012). In addition, in group I discs $T_{rot} < T_{vib}$, while in group II discs, $T_{vib} \lessapprox T_{rot}$ (van der Plas et al. 2012).

Furthermore, the line profile suggests that there has been CO depletion in the innermost regions of HAEBE discs (van der Plas et al. 2009), with group I clearing a larger radius ($r_{in} \sim 10$ AU) than group II discs ($r_{in} \sim 1$ AU; van der Plas et al. 2012). The *transitional disc* HD 141569A is distinctive owing to its low $T_{rot} \sim 250$ K, while its T_{vib} (~5600 K) is in a similar range of the hottest CO observed in HAEBEs, attributed to UV fluorescence (Brittain et al. 2007). Furthermore, Goto et al. (2006) showed that this disc has an inner clearing in CO up to a radius of 11 AU, which is comparable to the group I discs.

The ^{12}CO lines observed in the millimetre come from low J transitions of optically thick CO located in the outer disc surface. These pure rotational transitions of cold CO ($\Delta v = 0$) are routinely detected in HAEBE discs (e.g. Piétu et al. 2003; Dent et al. 2005). Earlier, the existence of Keplerian rotation in discs was confirmed with mm interferometry of CO lines (Koerner et al. 1993). Furthermore, as the lines are optically thick, a simple model of the line profile allows for an estimate of the outer disc radius and even inclination (e.g. Dent et al. 2005; Panic et al. 2008).

Woitke et al. (2010) calculated a grid of disc models with the thermo-chemical radiation code ProDiMo. This model grid, called "Disc Evolution with Neat Theory" is a useful tool for deriving statistically meaningful dependences on stellar and disc properties. Kamp et al. (2011) used the model grid to derive the line diagnostics that are relevant to the PACS observations. We refer to these diagnostics in our discussion below. Our sample includes several objects that appeared remarkable in earlier papers, in terms of their detections of H_2, CO, and/or OH, which can be attributed to a high level of UV fluorescence; we also relate these results to our new observations. We now discuss the results presented in the previous sections in the context of our current understanding of these discs. The following sections present our interpretation of observational correlations and their implications for the disc structure and evolution.

To remove the bias that can be introduced by the distance of the stars, we scaled our data to a distance of 140 pc (to ease comparison with objects in Taurus and the predictions of the model grid). The scaled data include all the PACS line and continuum fluxes, the ^{12}CO J = 3–2 and 2–1 line fluxes, and the mm continuum fluxes.

The relations between parameters are analysed with their corresponding "p-values" (see Table 7), which gives the probability that the two variables considered are not correlated. Two parameters are classified as "correlated" if one or more of the three (Spearman, Kendall, and Cox-Hazard) tests obtained p-values no higher than 1%, and as "tentatively correlated" when $1 < p < 5\%$ (e.g. Bross 1971). When $p > 5\%$, the parameters were classified as "not correlated", as their p-values were similar to the p-values derived for randomly generated samples. The p-values and linear fits provided in Table 7 take into account that several of our datasets include upper/lower limits instead of detections, as they were derived with the ASURV package (Feigelson & Nelson 1985; Isobe et al. 1986; Lavalley et al. 1992), which was specifically designed to deal with censored data. We used the Spearman's partial correlation technique to

Table 7. Probability p (in percentage) that the two parameters (x, y) under consideration are not correlated, calculated with several statistical methods: Spearman's, Kendall's, and Cox-Hazard's.

Parameters		p Spearman	p Kendall	p Cox-Hazard	Result	Linear fit: $y = a \times x + b$	
x	y					a	b
log [O I] 63 μm	log [O I] 145 μm	0.07	0.06	<0.1	Correlated	1.2 ± 0.21	1.8 ± 3.3
log [O I] 63 μm	log CO J18–17	0.06	0.03	<0.1	Correlated	0.64 ± 0.07	–7.1 ± 1.1
log L_{UV}	log [O I] 63 μm	0.33	0.32	–	Correlated	0.72 ± 0.20	–16.1 ± 0.1
log T_{eff}	log L_{UV}	0.05	<0.1	<0.1	Correlated	9.3 ± 0.2	–36.5 ± 4.4
log $L_{[OI]6300\ Å}$	log [O I] 63 μm	0.88	0.45	–	Correlated	0.83 ± 0.21	–12.4 ± 1 = 0.9
log $F_{63\ \mu m}$	log $F_{1.3\ mm}$	0.19	0.09	0.01	Correlated	0.72 ± 0.1	–0.20 ± 0.2
log $F_{63\ \mu m}$	log [O I] 63 μm	4.6	4.4	2.7	Correlated?		
log CO J 3–2	log [O I] 63 μm	3.7	2.4	–	Correlated?		
log T_{eff}	log [O I] 63 μm	4.7	3.5	1.6	Correlated?		
log $L_{PAH6.2\ \mu m}$	log [O I] 63 μm	6.6	4.4	–	Correlated?		
log $L_{Br\gamma}$	log [O I] 63 μm	4.6	4.4	–	Correlated?		
log CO J 2–1	log [O I] 63 μm	54	31	–	Not correlated		
log L_*	log [O I] 63 μm	7.2	9.2	18	Not correlated		
log L_X	log [O I] 63 μm	84	71	–	Not correlated		
log $F_{1.3\ mm}$	log [O I] 63 μm	34	27	44	Not correlated		
log L_{Acc} (BaDis)	log [O I] 63 μm	84	83	–	Not correlated		
log F_{IR}/F_*	log [O I] 63 μm	21	27	47	Not correlated		
slope b	log [O I] 63 μm	43	38	72	Not correlated		

Notes. Under "result" we indicate the results of these statistical tests.

quantify the influence of the common distance parameter on the probability of false correlation, finding that it is negligible for our sample – the p-values considering the distances, or random values instead, are practically equal. The absence of any influence of the distances on the correlations most probably comes from the relatively narrow range covered by this parameter in our sample. We excluded 51 Oph in the correlation test with L_{UV} and [O I] 63 μm, as it is both an outlier owing to its extremely high L_{UV} relative to the rest of the sample (see Table 2 and Fig. 8) and an enigmatic object (e.g. van den Ancker et al. 2001).

4.1. Oxygen fine-structure lines

In Fig. 6, we plot the strength of the [O I] 63 μm line as a function of the continuum flux at 63 μm. The variables are weakly correlated (see Table 7). The three sources with the highest line fluxes also have the highest continuum fluxes, namely AB Aur, HD 97048, and HD 100546, to which we refer as "the bright three". These are also the only HAEBEs in which H_2 emission has been detected in the IR (see Sect. 1).

The ratios of the fine-structure line fluxes of [O I] 63 μm, [O I] 145 μm, and [C II] 157 μm are diagnostics of the excitation mechanism (e.g. Kaufman et al. 1999). Unfortunately, for most of the sources we only obtained upper limits for one or more of these lines. We show the line flux of [O I] 63 μm as a function of [O I] 145 μm in Fig. 6, and find a clear correlation (see Table 7). We find line ratios of [O I] 63 μm to [O I] 145 μm between 10 and 30. These ratios are incompatible with predictions of the PDR model in Tielens & Hollenbach (1985) for optically thick lines with $T_{gas} < 200$ K. Our line ratios (which have a median of 24) agree with predictions from the model grid, which gives a median line ratio of 25 (Kamp et al. 2011). These authors conclude, based on those disc models, that the line ratio insensitive to the average oxygen gas temperature (for $50 < T_{gas} < 500$ K), but instead correlates with the gas-to-dust ratio.

4.2. Ionised carbon fine-structure line

The [C II] line flux is very sensitive to the UV radiation field, and the line is mostly optically thin. Unfortunately, most of our sources are background contaminated, as [C II] is also detected in off-source positions, in a variable amount, depending on the location. For the few sources with solid, non-[C II] background contaminated detections, we find line ratios of [O I] 63 μm/[C II] 157 μm between 10 and 30.

4.3. Carbon monoxide

Freeze-out of CO on grains is unexpected in the disc of an A-type star (e.g. Panic et al. 2009), so that the strength of the low-J ^{12}CO lines can be used to obtain a lower limit to the cold gas mass. The disc size can be derived from the ^{12}CO flux and profile. In Fig. 7, we plot the [O I] 63 μm line flux as a function of the ^{12}CO $J = 2$–1 and $J = 3$–2 line strengths (data from Dent et al. 2005; Panic et al. 2009; Isella et al. 2010; Öberg et al. 2010, 2011, and our own data, see Appendix B). We do not find a correlation with the $J = 2$–1 transition, but find a weak correlation with the $J = 3$–2 transition (see Table 7).

Kamp et al. (2011) showed that the ratio of [O I] 63 μm to ^{12}CO $J = 2$–1 can be used to derive the gas mass in the disc to an order of magnitude. The idea is that this ratio is determined by the average gas temperature in the disc. If the [O I] 63 μm line is optically thin, the line flux will depend mainly on the gas mass and average [O I] temperature (Woitke et al. 2010). Once the temperature is known, the line flux of [O I] 63 μm can thus be related to the disc gas mass. In our sample, we have nine sources for which the ^{12}CO $J = 2$–1 line flux is known. We calculated the ratio for those sources, and found that log ([O I] 63 μm/^{12}CO $J = 2$–1) falls between 2.5 and 3.5. This means that we have a similar average gas temperature in all cases. We applied the relation for this ratio range

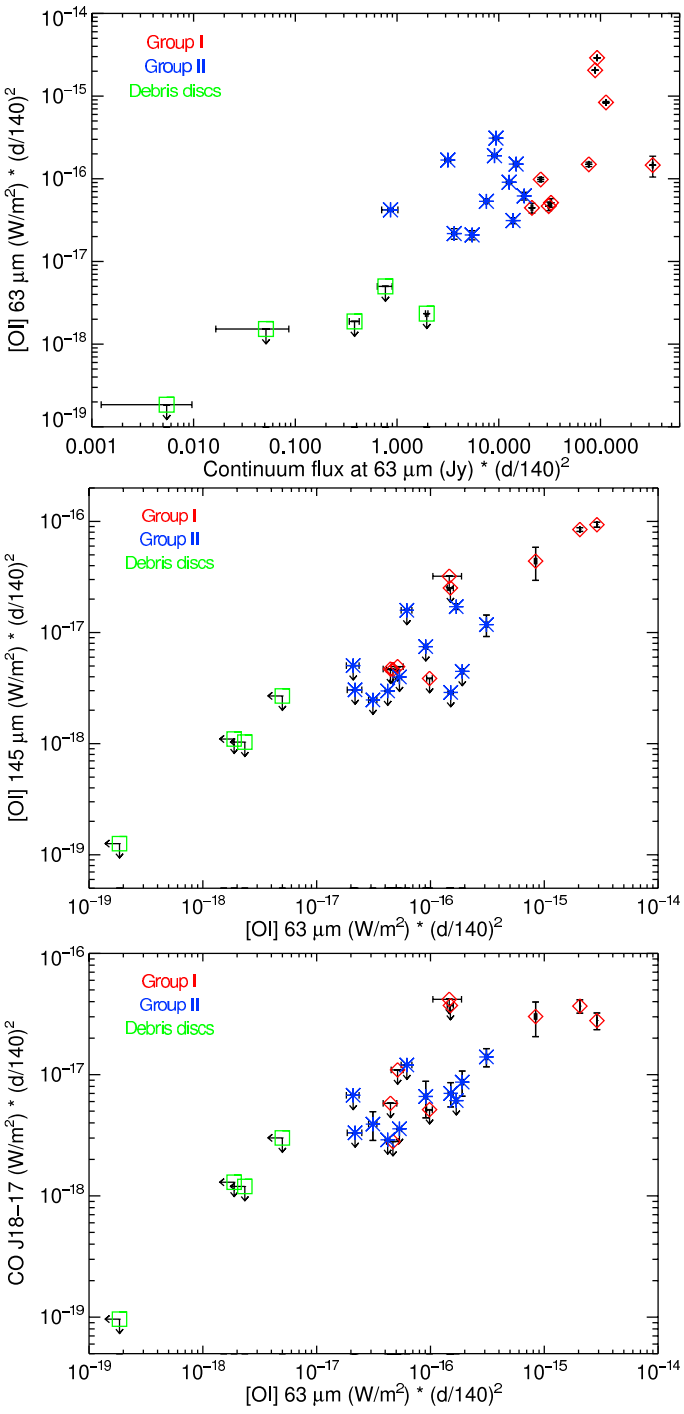


Fig. 6. *Top to bottom*: [O I] 63 μm as a function of the continuum flux at 63 μm; [O I] 145 μm as a function of [O I] 63 μm and CO J = 18–17 as a function of the [O I] 63 μm flux. All fluxes are normalised to a distance of 140 pc. Diamonds are group I sources, asterisks group II sources, and squares are debris discs.

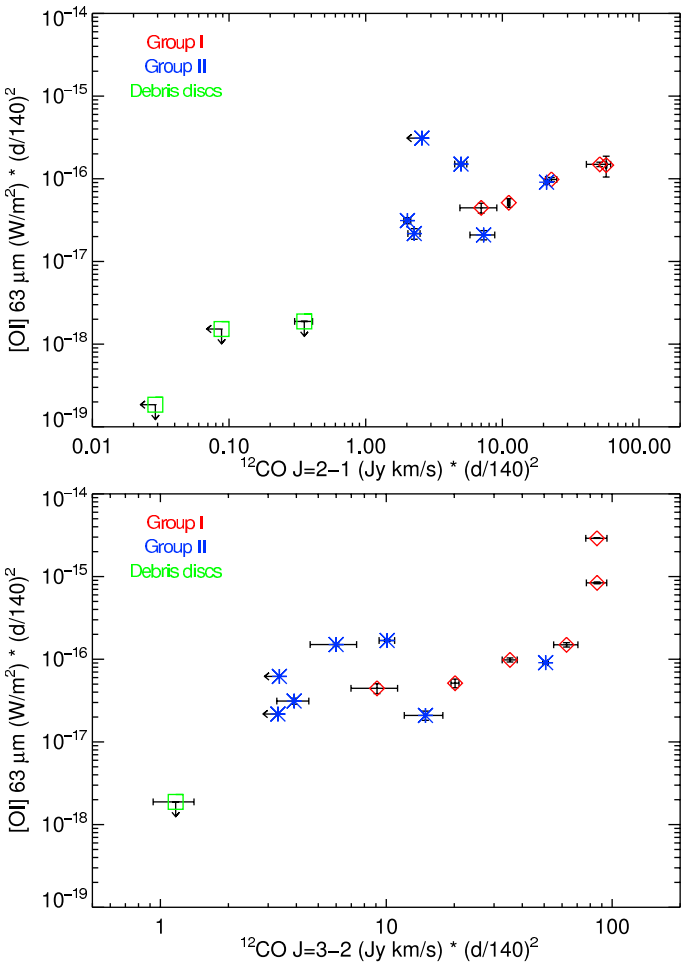


Fig. 7. [O I] 63 μm line flux versus strength of the ^{12}CO J = 2–1 (*top*) and J = 3–2 transitions (*bottom*). All fluxes are normalised to a distance of 140 pc. Diamonds are group I sources, asterisks group II sources, and squares are debris discs.

between log [O I] 63 μm and the gas mass, derived by Kamp et al. (2011) to obtain an estimate of the disc mass. The results are shown in Table 8. We derived values of $M_{\rm gas}$ between 0.24 $M_\odot$ and 25 $\times$ 10^{-3} $M_\odot$. These values are of course only indicative; for a more accurate estimate, a full model of all the available observations needs to be developed for each disc. The masses are consistent with the estimates derived from detailed modelling of HD 163296 ($M_{\rm gas}$ ~ 15–120 $\times$ 10^{-3} $M_\odot$; Tilling et al. 2012) and HD 169142 ($M_{\rm gas}$ ~ 3–7 $\times$ 10^{-3} $M_\odot$; Meeus et al. 2010).

Table 8. Line fluxes of ^{12}CO J = 2–1, log of the line ratios, and derived gas masses.

Object	^{12}CO J = 2–1 (10^{-18} W/m^2)	log ([O I] 63 μm/ CO J = 2–1)	$M_{\rm gas}$ ($M_\odot$)
HD 31648	0.169	2.75	6.5×10^{-3}
HD 35187	0.026	3.10	2.5×10^{-3}
HD 36112	0.099	2.58	0.24×10^{-3}
CQ Tau	0.024	3.30	4.4×10^{-3}
HD 135344 B	0.080	2.78	2.2×10^{-3}
HD 139614	0.054	2.92	2.2×10^{-3}
HD 142527	0.160	2.52	0.66×10^{-3}
HD 142666	0.052	2.57	0.62×10^{-3}
HD 163296	0.053	3.59	25.4×10^{-3}
HD 169142	0.164	2.75	5.3×10^{-3}
49 Cet	0.015	2.84	$<3.3 \times 10^{-3}$

4.4. Hydroxyl

Although less abundant than H_2 and CO, hydroxyl (OH) is also an important molecule, as it plays a central role in the formation/destruction of H_2O, H_2, and [O I]. Mandell et al. (2008) were the first to detect ro-vibrational transitions of warm OH (at 3.0–3.7 μm) in two HAEBEs, AB Aur and HD 36112.

They derived a rotational temperature of 650–800 K, and argue that fluorescent excitation is responsible for the emission of OH located in the disc surface layer. Fedele et al. (2011) also searched for OH in 11 HAEBEs with CRIRES, detecting it in 4 sources with spectral types between B5 and A1; none of those objects are in our sample. They found that objects with an OH detection tend to be Meeus group I sources. More recently, several transitions of OH around 3 μm were detected in HD 100546 (Liskowsky et al. 2012). In our PACS spectra, we only detect OH in HD 163296 (and a tentative detection in AB Aur); however, we only cover one doublet, which is not the strongest in the far-IR, hence our data may be insufficiently deep. Sturm et al. (2010) detected several OH lines in their full SED range mode PACS spectra of HD 100546, among which the 84 μm doublet is the strongest. In our spectrum at 79 μm, we find evidence of the OH doublet, although not a 3σ detection (see Fig. 5).

4.5. Water

The detection of water has never been reported to be detected in a Herbig Ae/Be disc despite several searches in the near- and mid-IR (e.g. Pontoppidan et al. 2010; Fedele et al. 2011). However, in the study of Pontoppidan et al. (2010), HD 163296 was found to display a H_2O emission line at 29.85 μm, although water was only confirmed to be present in that paper when detected at both 15.17 μm and 17.22 μm, with at least 3.5σ confidence.

Thi & Bik (2005) showed that the ratio H_2O/OH declines when the ratio of the UV field intensity to the density increases. Thus, in lower density regions with a lot of UV radiation, the amount of water expected is low, relative to OH. Fedele et al. (2011) conclude that, if water vapour is present, it must be located in deeper, colder layers of the disc than where OH originates; the disc atmosphere is depleted in water molecules.

We detected at least one water line and evidence of several others in HD 163296, which is a group II source. Tilling et al. (2012) modelled the disc of HD 163296 based on our earlier, shallower, range scans, and showed that the disc is mostly settled, which results in slightly warmer dust and increased line flux. This fact, together with the rather high UV luminosity, can probably explain the water detections in this disc.

Kamp et al. (2011) found that strong dust settling will increase the water abundance at the disc surface. The reason is complex (we refer the reader to Sect. 5.3 of Kamp et al.), but the main idea is that there is an efficient cold-water formation route in these discs. We note that HD 100546, the source that has the highest UV flux and is richest in other, strong lines ([O I] 63 μm, CO and CH^+), does not show evidence of warm water. HD 100546 is a group I source, which is thought to have had its inner disc cleared (e.g. Bouwman et al. 2003; Benisty et al. 2010). Woitke et al. (2009b) showed that water lines originate in three distinct regions: 1) a deep midplane behind the inner disc wall, up to 10 AU, hosting most of the water vapour; 2) a midplane region between 20 AU and 150 AU where water freezes out and there is a small amount of cold water vapour; and 3) a warm water layer between 1 AU and 50 AU higher up in the disc. In the disc of HD 100546, region 1 and part of region 3 are missing owing to the presence of a gap, so that the amount of gas phase water is much smaller than what is predicted for a full disc.

Furthermore, while in the inner disc of HD 163296 the density is too low for water to form (from OH + H_2) to balance the fast photodissociation (see e.g. Thi & Bik 2005), water can survive in the inner 10 AU of the warm atmosphere. In contrast, in the UV-strong star HD 100546, even at 30 AU the UV field is too strong for water to survive. This, in combination with the greater amount of settling in the HD 163296 disc, might explain the absence of detectable warm H_2O emission in the disc of HD 100546 while it is detected in HD 163296.

4.6. CH^+

The formation of CH^+ is controlled by the gas-phase reaction $C^+ + H_2 \rightarrow CH^+ + H$, which has an activation energy of 4500 K. Hence, CH^+ not only traces the presence of H_2 but also the presence of hot gas. In our sample, IR molecular hydrogen was detected in three targets (see Sect. 1): AB Aur, HD 97048, and HD 100546. In two of these objects, we also detect CH^+, suggesting that their formation and excitation mechanisms are indeed related. For a more in-depth discussion of CH^+ in HD 100546, we refer to Thi et al. (2011).

5. Correlations of [O I] 63 μm line flux with stellar and disc parameters

In the next few paragraphs, we describe our search for correlations between the observed [O I] 63 μm line fluxes and the properties of the objects. For this study, we did not include the debris discs, as these have a very different nature. In addition, we were unable to detect any [O I] 63 μm line from these discs, so that we would only be able to compare with upper limits for this line.

5.1. The influence of T_{eff} and both UV and X-ray luminosities

We searched for a correlation between stellar parameters and the [O I] 63 μm line flux. We found no trend between either age or stellar luminosity and the line flux. In Fig. 8, we show the relation between the line flux of [O I] 63μm and the effective temperature of the stars. Both appear to be uncorrelated, until $T_{\rm eff}$ reaches 10 000 K, when the [O I] 63 μm flux increases dramatically for a few sources. Our p-values (see Table 7) are inconclusive, hence the significance of any correlation cannot be established from our statistical analysis.

The UV and X-ray photons play an important role in the chemistry and temperature balance of protoplanetary discs. For HAEBEs, the UV photons are important in heating the disc, through their absorption by PAHs and the subsequent photoelectric effect. In Fig. 8, we show the relation between the line flux of [O I] 63 μm, the UV luminosity calculated from IUE spectra (see Sect. 2), and the X-ray luminosity (data mainly found in Hubrig et al. 2009, see Table C.1 for a full list). There is a clear correlation between the [O I] 63 μm flux and the UV luminosity (see Table 7), as reported earlier for a limited sample in Pinte et al. (2010). This could be related to an increase in OH photo-dissociation in the disc surface and/or to a more efficient photoelectric heating of the gas by PAHs in sources with a higher UV luminosity.

X-ray photons can ionise both atoms and molecules. The X-ray fluxes observed in HAEBEs (log $L_{\rm X}$ = 28–30) are on average lower than those of the lower-mass T Tauri stars (TTS; log $L_{\rm X}$ = 29–32). Aresu et al. (2011) found from theoretical modelling of discs a correlation between the X-ray luminosity and the [O I] 63 μm line flux for X-ray luminosities

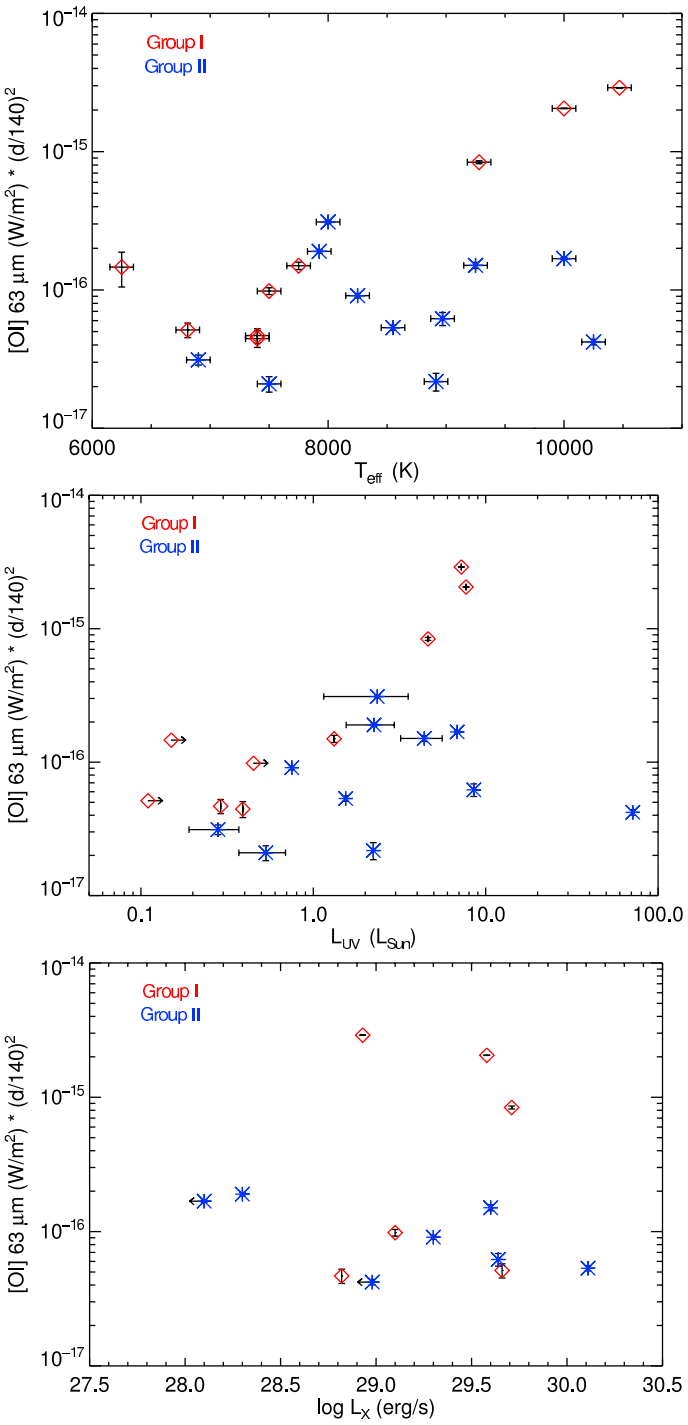


Fig. 8. [O I] 63 μm versus effective temperature, UV luminosity and X-ray luminosity. Diamonds are group I sources, asterisks are group II sources.

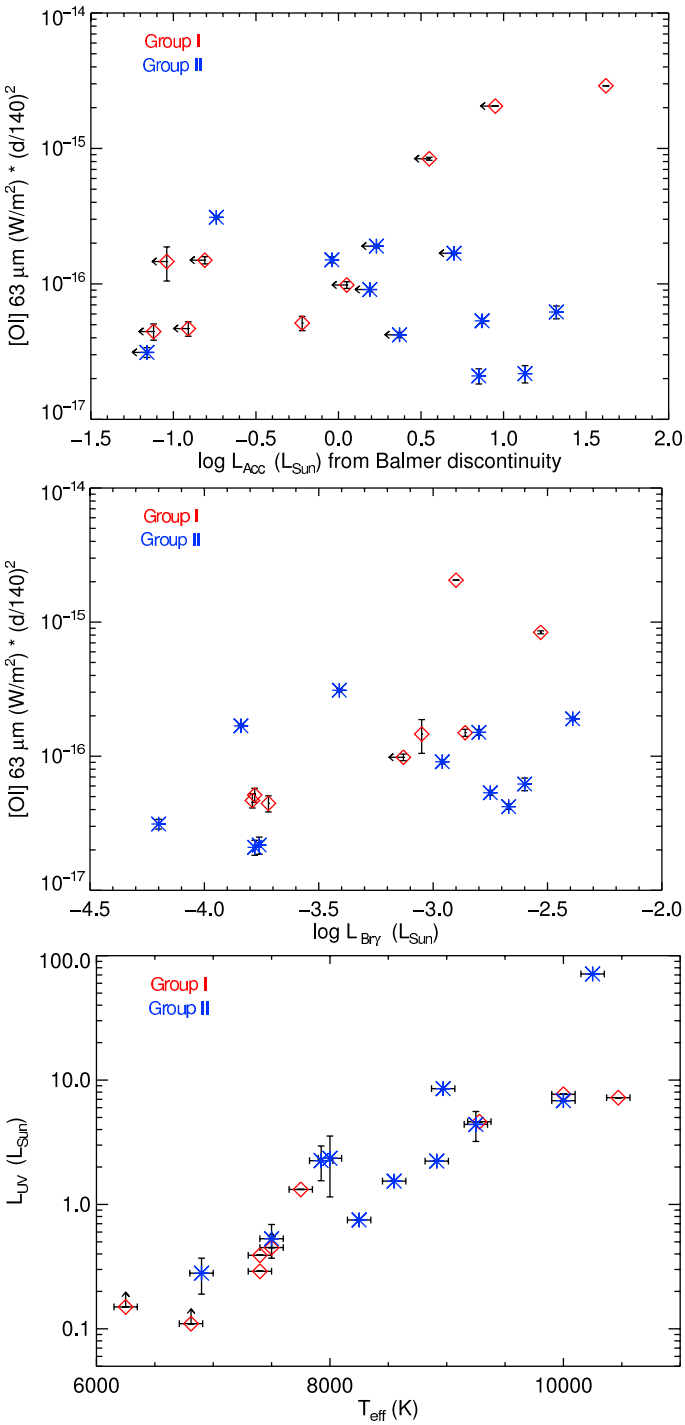


Fig. 9. *Top*: [O I] 63 μm versus the accretion rate derived from the excess in the Balmer discontinuity. *Middle*: [O I] 63 μm versus the luminosity of the Br$_\gamma$ line. *Bottom*: $L_{\rm UV}$ vs. $T_{\rm eff}$. Diamonds are group I sources, asterisks are group II sources.

above 10^{30} erg/s. Below that value, the gas temperature in the region where the [O I] 63 μm line forms is dominated by UV heating, while above that value X-rays provide an additional heating source, thereby increasing the total line flux. Since all objects in our sample are below this L_X threshold, it is unsurprising that we do not see a correlation with the X-ray luminosity. Furthermore, X-rays in HAEBEs are softer than in TTS, so that they cannot penetrate as deeply in the discs as in T Tauri discs. A dedicated study will use spectral X-ray properties to interpret the observed PACS spectra (Güdel et al., priv. comm.).

5.2. Relation of [O I] 63 μm line flux with accretion rate

In Fig. 9, we plot the line flux of [O I] 63 μm as a function of $L_{\rm acc}$ derived from the excess in the Balmer discontinuity. No trend is visible, just more scattering at higher $L_{\rm acc}$. However, we highlight the difficulties that lie in an accurate determination of the accretion rate, and introduce additional scatter in the values. We also plot the [O I] 63 μm line flux against the Brγ luminosity (data from García-Lopez et al. 2006; Donehew et al. 2011). Here

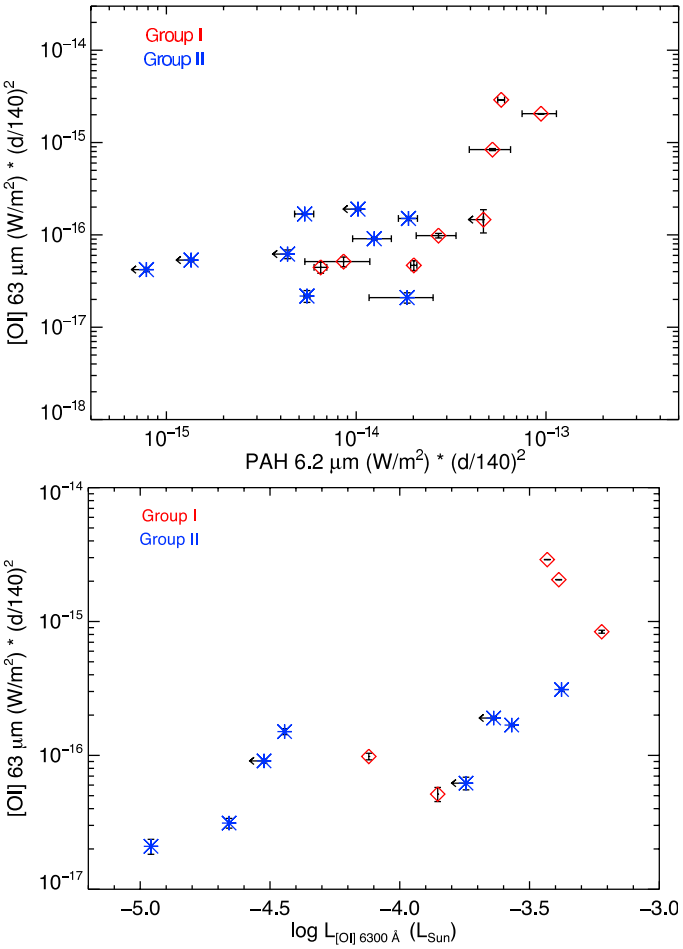


Fig. 10. *Top*: [O I] 63 μm line flux versus PAH 6.2 μm line flux. *Bottom*: [O I] 63 μm line flux versus the luminosity of [O I] 6300 Å. Diamonds are group I sources, asterisks are group II sources.

we see a tentative correlation with $L_{\rm Bry}$. Given that we do not see a clear correlation between the accretion rate and the [O I] 63 μm line flux, we can conclude that the accretion is not an important contributor to the excitation of [O I] 63 μm in HAEBEs. This confirms the findings of an earlier study of a few HAEBEs by Pinte et al. (2010), that the emission from HAEBE discs can be explained by photospheric heating alone. In Fig. 9, bottom, we plot $L_{\rm UV}$ versus $T_{\rm eff}$, and see that both are very well correlated. This means that the bulk of the UV luminosity in HAEBEs is photospheric, rather than originating in accretion, as is often observed in the cooler T Tauri stars (e.g. Yang et al. 2012).

5.3. Relation to both PAH and [O I] 6300 Å emission

Polycyclic aromatic hydrocarbons are important for the heating of the disc by means of the photo-electric effect. In HAEBEs, the PAH luminosity, $L_{\rm PAH}/L_*$ is observed to reach up to 9×10^{-3}. In Fig. 10, we show the relation between the PAH luminosity and the [O I] 63 μm line fluxes (data from Acke et al. 2004b; Keller et al. 2008). The [O I] 63 μm flux and the PAH flux weakly correlate with each other (see Table 7).

HD 141569A is the only star for which we detected [O I] 145 μm, but not CO at 144.8 μm. The [O I] 63 μm to [O I] 145 μm flux ratio is smaller than 10, while it is around 20 in AB Aur, HD 97048, and HD 100546. Moreover, Brittain et al. (2007) showed from CO 4.7 μm modelling that $T_{\rm rot}$ is of the order of 250 K, while $T_{\rm rot}$ in HD 97048 and HD 100546 is much higher, ≥1000 K. This difference cannot be attributed to a lower UV luminosity as it is rather similar (6.83 $L_\odot$ in HD 141569A versus 7.69 $L_\odot$ in HD 97048 and 7.22 $L_\odot$ in HD 100546). However, a lower PAH luminosity is observed in HD 141569A (a factor of ten less; Acke et al. 2010), so there is a smaller heat contribution to the disc. There might also be an intrinsic difference in PAH abundance.

The excitation mechanism of [O I] 6300 Å is still not well-determined: it could be either thermal or non-thermal (e.g. fluorescence or OH photodissociation). The emission line is commonly found in HAEBEs (e.g. Corcoran & Ray 1998). Acke et al. (2005) derived from a simple model of the spectroscopically resolved [O I] 6300 Å line, that the emission originates from the disc surface, assuming that it is non-thermally excited by the UV photo-dissociation of OH molecules in the disc surface. It is more often found in flared than self-shadowed discs (Acke et al. 2005) and traces the disc between 0.1 AU and 50 AU (van der Plas et al. 2009). In the bottom plot of Fig. 10, we plot [O I] 63 μm against [O I] 6300 Å data from Acke et al. (2005), van der Plas et al. (2008), and Mendigutía et al. (2011a). Here we see a correlation that could be explained by the excitation mechanism of both lines being related to UV photons. We have already shown that there is no obvious correlation between the accretion rate and the [O I] 63 μm line strength. The unusual properties of the "bright three" objects, which have high UV luminosities based on their high line fluxes of [O I] 63 μm and PAH luminosity, thus must mainly be the result of their higher effective temperatures than the rest of the sample. The only other objects in our sample with a temperature of around 10 000 K, are HD 141569A (a transitional disc) and 51 Oph, which is a special case with a sharp drop in the SED at longer (>20 micron) wavelengths, which can be attributed to a compact disc in which the dust has settled towards the midplane.

5.4. Relation to with disc properties

The continuum flux at 1.3 mm is often used to derive a minimum dust mass of the disc, under the assumption that the dust emission is optically thin (Beckwith et al. 1990). In Fig. 11, we plot the [O I] 63 μm flux as a function of the continuum flux at 1.3 mm (our mm data collected in the literature are listed in Appendix C.2; we also use our own unpublished SMA data, see Appendix B). We did not find that these variables are correlated (see Table 7). On the other hand, the continuum flux at 63 μm and at 1.3 mm are strongly correlated (see Fig. 11).

In Fig. 12, we plot the line flux of [O I] 63 μm as a function of the total IR excess, which is a proxy for the amount of dust continuum observed. We do not find a correlation. This is likely because the IR continuum is rather a tracer of the dust disc, and the scale height of the gas disc may be higher than that of the dust, as already observed in a few HAEBEs (e.g. van der Plas et al. 2009). HD 141569A has a transitional disc, with a much smaller $F_{\rm IR}/F_*$ than the rest of the sample (see Table 2), indicating that the disc is barely flaring and perhaps has already dissipated much of its disc material. All these diagnostics lead us to confirm that the disc of HD 141569A differs considerably (inner disc mostly cleared of dust) from that of HD 97048 and HD 100546, which still have flaring gas-rich discs. Modelling of the HD 141569A disc with ProDiMo will help us to better understand these differences in terms of excitation mechanisms,

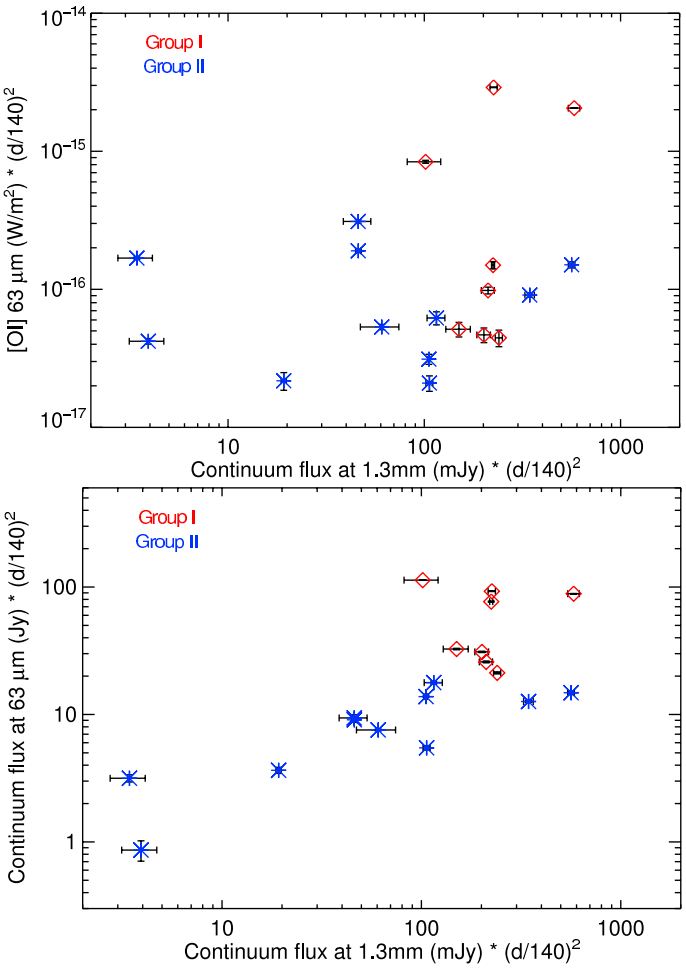


Fig. 11. *Top*: [O I] 63 μm versus the continuum flux at 1.3 mm; there is a weak trend of stronger line flux with higher continuum flux. *Bottom*: the continuum flux at 63 μm versus the continuum flux at 1.3 mm, where we see a strong correlation. Diamonds are group I sources, asterisks are group II sources.

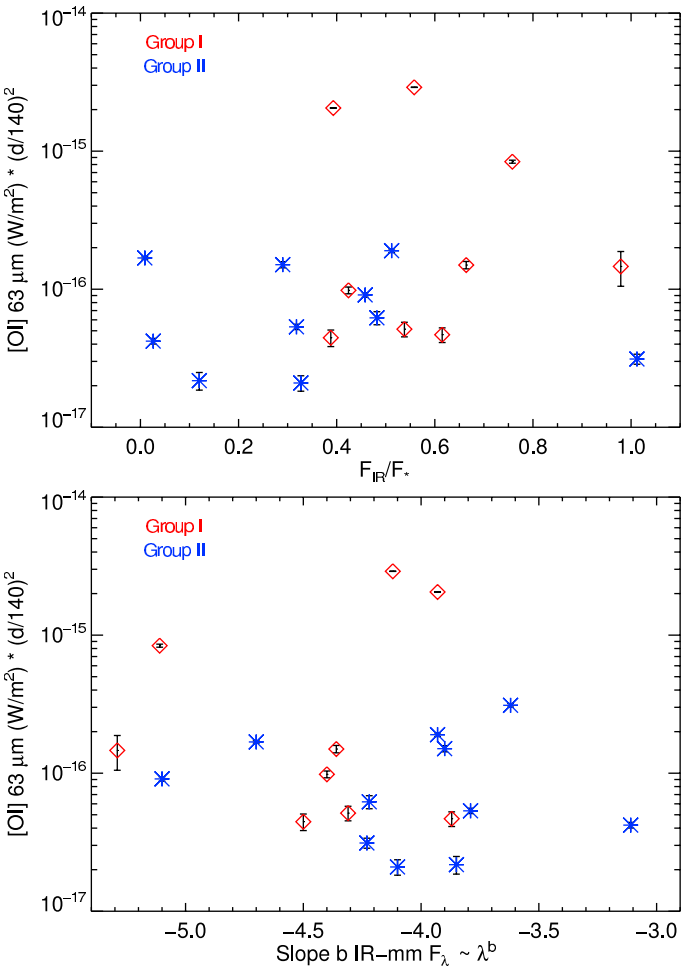


Fig. 12. *Top*: [O I] 63 μm line flux versus amount of IR excess. We find no correlation between these variables. The two objects to the left are HD 141569A and 51 Oph, a transitional and a compact disc, respectively. *Bottom*: [O I] 63 μm line flux versus the slope b of the SED at far-IR to mm wavelengths. The line flux also does not correlate with the SED slope. Diamonds are group I sources, asterisks are group II sources.

amount of gas, and disc structure (Thi, in prep.). Our data suggest that, in HD 141569A, the CO is located deeper in the disc (closer to the dust) where it can be thermalised and/or shielded from photodissociation by direct UV photons.

The slope b of the far-IR to mm SED, where $F_\lambda \sim \lambda^b$, can be related to the size of the dust grains radiating at mm wavelengths. However, grain size is not the only factor influencing the slope: both the composition (e.g. amount of carbon) and grain shape can also be important factors. Acke et al. (2004a) showed that the SED far-IR to mm slope is related to the SED group: self-shadowed discs (group II) have on average shallower slopes than their flaring counterparts (group I). In our sample, we do not see a correlation between the [O I] 63 μm line strength and the SED slope (see Fig. 11).

5.5. Non-detections in debris discs

In our sample, we have five debris discs for which the [O I] 63 μm line was not detected. We obtain 3σ upper limits for the [O I] 63 μm line flux (at their respective distances) $\sim$6–10 $\times$ 10^{-18} W/m^2. This contrasts with the young debris disc β Pic, where [O I] 63 μm and [C II] 158 μm emission lines were detected with *Herschel*/PACS (Brandeker et al. 2012). These authors give an [O I] 63 μm line flux =13.2 $\times$ 10^{-18} W/m^2 for β Pic (at a distance of 19 pc), which would not have been detected at the distance of our debris discs. The only exception is HR 1998, at a distance of 22 pc, for which we have an upper limit $\sim$5 $\times$ 10^{-18} W/m^2 when scaled to 19 pc, which is almost a factor of three lower than the β Pic detection. β Pic appears to be a special debris disc that is relatively rich in gas, originating from the ongoing vaporisation of dust through grain-grain collisions, comet evaporation, and/or photo-desorption of grain surfaces (Lagrange et al. 1998; Czechowski & Mann 2007; Chen et al. 2007).

6. Conclusions

In this paper, we have studied with *Herschel*/PACS spectroscopy the gas content of 20 HAe stars and 5 A-type debris discs, which can be summarised as follows:

1. We have detected the [O I] 63 μm line in all the HAe stars of our sample, while it is absent in the debris discs, confirming the lack of a large amount of gas in these discs. The [O I] 63 μm line is by far the strongest line observed

in our spectra, next in strength (if detected) are [O I] 145 μm and [C II]; they are only detected in 5 (25%) and 6 (30%) sources, respectively.
2. The CO mid to high J transitions (18–17 and 29–28) are only detected in 9 (45%) and 2 (10%) objects, respectively. The highest J (33–32 and 36–35) CO lines covered in our spectra are not seen at all in our sample. The three detections of CO J = 29–28 are in the three strongest UV emitting objects, AB Aur, HD 97048, and HD 100546, revealing the need for a large amount of UV photons for this line to become visible. Interesting in this respect is the transitional disc of HD 141569A, where we did not detect CO J = 18–17, but did detect a strong line of [O I] 145. This cannot be attributed to a difference in UV luminosity but rather to significant inner disc clearing, and a more tenuous disc.
3. We have detected two lines of CH^+ in HD 100546, and also CH^+ at 90.02 μm for the first time in HD 97048, only the second HAe star in which CH^+ is detected.
4. Hydroxyl and H_2O are important ingredients of the disc chemistry. However, we found water and OH in only one object, HD 163296, which has a settled disc. The previous detection of H_2O, announced by Sturm et al. (2010) in HD 100546 cannot be confirmed. This misidentification was caused by a blend with the CH^+ line, which is often present at the same wavelength as H_2O. The non-detection of H_2O in most sources agrees with findings of Pontoppidan et al. (2010) and Fedele et al. (2011), who also did not detect water at IR wavelengths, despite their dedicated surveys.

We were able to correlate the strength of the [O I] 63 μm line with stellar parameters, as well as disc properties. We can summarise our findings as follows:

1. The [O I] 63 μm line flux correlates weakly with the continuum flux at 63 μm. The line flux ratios of [O I] 63 μm to [O I] 145 μm and [O I] 63 μm to [C II] are between 10 and 30.
2. We found that three of our sources, AB Aur, HD 97048, and HD 100546, have very strong [O I] 63 μm line fluxes, relative to the rest of the sample. These three sources have group I discs and the highest $T_{\rm eff}$ values in the sample, thus the highest stellar UV fluxes. We indeed see a correlation between the *total* (stellar + accretion) UV luminosity and the strength of the [O I] 63 μm line. We do not see a correlation between this strength and the X-ray luminosity, which is rather low in our sample of HAEBE stars.
3. We did not find a correlation between the line flux and the accretion rate estimated from the Balmer discontinuity, but did find a tentative one between the line flux and the Brγ line. This shows that accretion is not the main driver of the [O I] 63 μm excitation in HAEBEs. The bulk of the UV luminosity is photospheric rather than caused by accretion.
4. Sources with high [O I] 63 μm fluxes also have high PAH luminosities, where both may be related to their high UV fluxes. We also see a correlation with the luminosity of the [O I] 6300 Å line.
5. The disc geometry (flat versus flared) does not uniquely determine the strength of the [O I] 63 μm line flux. The three strongest lines are observed in flared discs, but once these sources are excluded, there is no significant difference in line strength observed between the group I and II discs.
6. We found a strong correlation between the continua at 63 μm and 1.3 mm. There is no correlation between the [O I] 63 μm line strength and the strength of the dust continuum at 1.3 mm. We also found no correlation between the line flux and either the slope of the far-IR to mm SED, or the IR excess.
7. We see a weak correlation with the strength of ^{12}CO J = 3–2 line. On the basis of the line ratio [O I] 63 μm/^{12}CO J = 2–1, we were able to estimate the gas mass present in the disc. We found a $M_{\rm gas}$ between 0.25 $M_\odot$ and 25 $\times$ 10^{-3} $M_\odot$, which is consistent with the estimates derived from a detailed modelling of HD 163296 ($M_{\rm gas}$ $\sim$ 15−120$\times$$10^{-3}$ $M_\odot$; Tilling et al. 2012) and HD 169142 ($M_{\rm gas}$ $\sim$ 3−6.5$\times$$10^{-3}$ $M_\odot$; Meeus et al. 2010).

A picture emerges for the protoplanetary discs around HAEBEs where the stellar UV flux is the main parameter controlling the strength of the [O I] 63 μm line, which is formed just below the disc surface. An increased amount of settling can enhance the line flux for species (such as water) that are formed deeper in the disc, where the density is higher. We plan to follow-up on this study with detailed modelling of a few key objects: AB Aur and HD 97048; and HD 135344 B and HD 142527 (group I, high and low UV, respectively), HD 163296 (group II), HD 141569 A (transitional disc), and finally the enigmatic compact disc of 51 Oph. Our modelling results will further aid in the understanding of the chemistry and physical processes present in Herbig Ae/Be discs.

Acknowledgements. We would like to thank the PACS instrument team for their dedicated support and A. Carmona for discussions about gas line diagnostics. G. Meeus, C. Eiroa, I. Mendigutía, and B. Montesinos are partly supported by AYA-2008-01727 and AYA-2011-26202. G. Meeus is supported by RYC-2011-07920. C.A.G. and S.D.B. acknowledge NASA/JPL for funding support. W.F.T. thanks CNES for financial support. F.M. thanks the Millennium Science Initiative (ICM) of the Chilean ministry of Economy (Nucleus P10-022-F). F.M., I.K., and W.F.T. acknowledge support from the EU FP7-2011 under Grant Agreement No. 284405. C.P. acknowledges funding from the EU FP7 under contract PERG06-GA-2009-256513 and from ANR of France under contract ANR-2010-JCJC-0504-01. PACS has been developed by a consortium of institutes led by MPE (Germany) and including UVIE (Austria); KUL, CSL, IMEC (Belgium); CEA, OAMP (France); MPIA (Germany); IFSI, OAP/AOT, OAA/CAISMI, LENS, SISSA (Italy); IAC (Spain). This development has been supported by the funding agencies BMVIT (Austria), ESA-PRODEX (Belgium), CEA/CNES (France), DLR (Germany), ASI (Italy), and CICT/MCT (Spain). This research has made use of the SIMBAD database, operated at CDS, Strasbourg, France.

Appendix A: PACS observation identifications

In Table A.1, we show the *Herschel* observation identification numbers (obsids) of our observations. Several stars were observed twice in the range mode, to obtain a deeper observation. These are also indicated in the table. In Figs. A.1–A.3, we show all the stars at 72, 79, and 180 μm.

Appendix B: Additional millimetre observations

Interferometric observations of HD 32297, HD 35187, HD 142666, HD 144668, HD 158352, HR 1998, and KK Oph were carried out in five tracks with the Sub-Millimeter Array (SMA; Ho et al. 2004) in the compact configuration from November 2010 to October 2011. The observations were carried out at a central frequency of 223.9 GHz, with upper and lower bandpasses of 4 GHz bandwidth and the centre of each bandpass was offset from the central frequency by 2.5 GHz. The continuum was sampled at 3.25 MHz, and 104 MHz regions were

Table A.1. Overview of the obsids that were observed.

Star	Line Spec	Range Spec
HD 9672	1342188424	1342188423
AB Aur	1342191355	1342191354
		1342226000 (D2)
HD 31648	1342226002	1342226003
HD 32297	1342217849	1342217850
HD 35187	1342226900	1342226901
HD 36112	1342227635	1342227636
HD 36910	1342227638	1342227637
HR 1998	1342226192	1342226193
HD 97048	1342188436	1342188435
HD 100453	1342203059	1342203058
	1342212228	1342203442
HD 100546	1342188438	1342188437
HD 104237	1342212234	1342212233
HR 4796A	1342199242	1342199243
		1342234488 (D1)
HD 135344B	1342190370	1342190369
HD 139614	1342191300	1342191299
HD 141569	1342190376	1342190375
		1342204340 (D3)
HD 142527	1342216173	1342216172
HD 142666	1342214224	1342214225
HD 144668	1342192146	1342216200
HD 150193	1342216625	1342216626
KK Oph	1342192148	1342192149
		1342228205 (D2)
HD 158352	1342190377	1342227800 (D1)
HD 158643	1342217821	1342217822
HD 163296	1342192161	1342192160
		1342229742 (D3)
HD 169142	1342186310	1342186309
		1342215676 (D2)

Notes. (D) means that it was a deeper observation than our regular settings. (D1) indicating settings at 79/158 μm, (D2) settings at 72/145 μm and 79/158 μm and (D3) all three range settings.

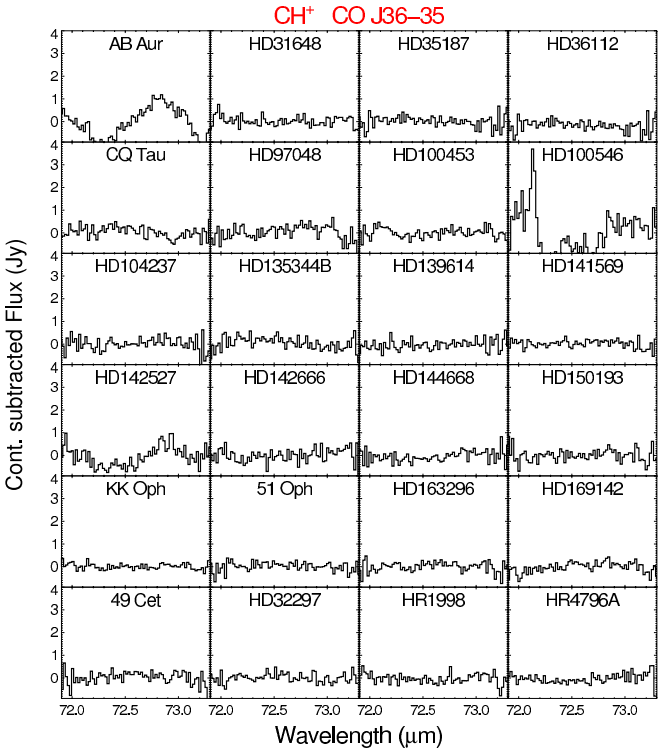


Fig. A.1. The region around 72 microns.

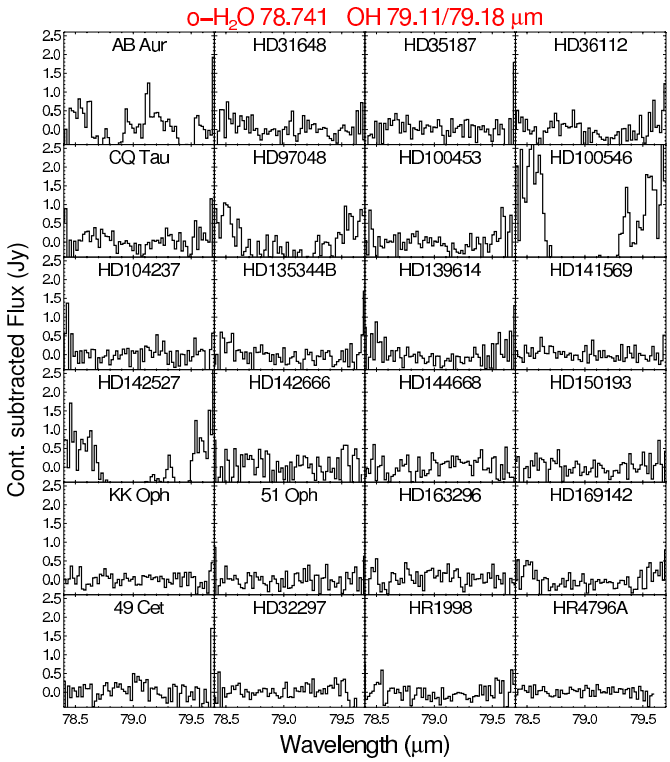


Fig. A.2. The region around 79 microns.

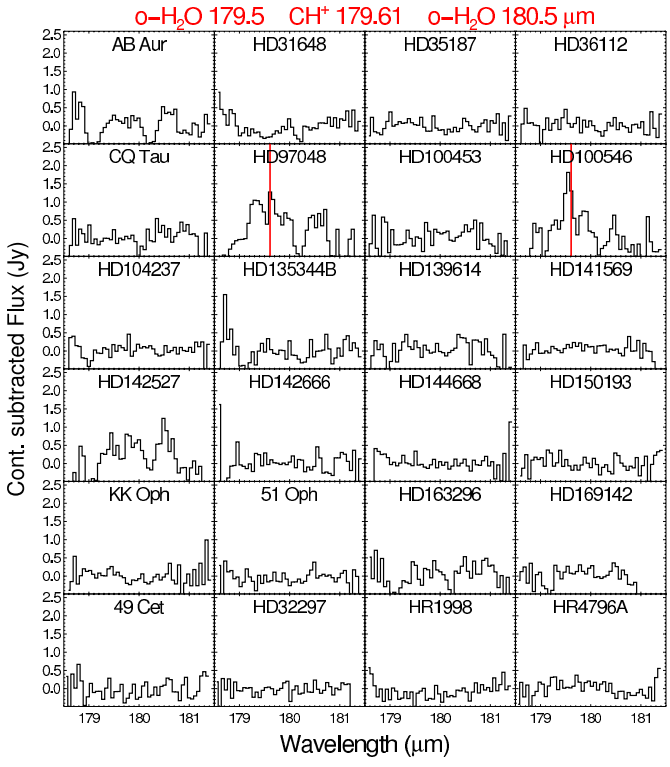


Fig. A.3. The region around 180 microns. With a vertical line, we indicate the position of CH^+.

set aside for 0.203 MHz resolution observations of the CO J = 2–1 line (230.538 GHz) line. The compact array observations included seven or eight antennas, with baselines of 10–70 m. Each object was observed for ~2.5 h total integration time in good

Table B.1. ^{12}CO 2–1 and ^{12}CO 3–2 line fluxes observed with SMA.

Star	^{12}CO 2–1 (Jy km s^{-1})	Error	^{12}CO 3–2 (Jy km s^{-1})	Error
HD 35187	<0.55	–	–	–
HD 142666	<0.62		–	–
HD 144668	confused		confused	
KK Oph	<1.08	–	–	–
HR 1998	<1.17	–	–	–
HD 158352	<0.48	–	–	–

Table B.2. Continuum fluxes at 1.2 mm, observed with MAMBO and at 1.3 mm, observed with SMA.

Star	$F_{1.2\ \mathrm{mm}}$ (mJy)	Error	$F_{1.3\ \mathrm{mm}}$ (mJy)	Error
HD 32297	3.14	0.822	3.10	0.74
HD 35187	33.960	1.001	28.95	0.85
HD 141569 A	4.785	0.507	–	–
HD 142666	102.500	2.022	99.0	4.3
HD 144668	–	–	34.3	0.9
HD 151093	47.860	2.091	–	–
KK Oph	36.160	2.260	24.5	4.3
51 Oph	5.007	0.599	–	–
HR 4796 A	–	–	<9.3	–
HD 158352	–	–	<0.7 5	–

conditions (zenith $\tau_{225\ \mathrm{GHz}}$ 0.06–0.25) with system temperatures of ∼100–230 K.

For gain calibration, we interleaved 5 min observations of close quasars between 20 min observations of the targets. We combined observations of two or three targets per track. We used 60–90 min observations of bright quasars for bandpass calibration, and 20 min observations of available planets for flux amplitude calibration. Observations of flux and bandpass calibrators were carried out before or after our targets were available. We flagged and calibrated the data using standard routines in the facility IDL package MIR. We carried out baseline-based phase-calibration, finding rms phase errors of ∼10–20°. On the basis of variations in the measured fluxes of our gain calibrators, the flux calibration has an uncertainty of ∼15%.

To measure the 1.3 mm continuum flux, we combined wide band continuum channels from all observations and both sidebands for each object. We used the MIRIAD command "uvfit" to fit a point source to each observation. To confirm that sources were unresolved in our observations, we carried out standard Fourier inversion, CLEAN deconvolution, and image reconstruction using natural weighting with the facility reduction tool MIRIAD. The typical synthesized beam of the combined observations is ∼3.″5 × 2.″8, with an rms of 0.3–1.5 mJy/beam in the continuum. We separately carried out the same imaging process on the higher spectral-resolution line data, binning in 1.0 km s^{-1} velocity channels centred on the CO $J = 2 \rightarrow 1$ line. The beam size is slightly smaller than in the continuum, with a rms in each channel from 0.4 to 2 Jy/beam. We list the line fluxes in Table B.1 and the 1.3 mm continuum fluxes in Table B.2.

In addition, HD 32297, HD 35187, HD 142666, KK Oph, HD 141569, HD 150193, and HD 158643 were observed for continuum emission at 1.2 mm using the MAMBO2 bolometer array (Kreysa et al. 1998) on the IRAM 30m telescope at Pico Veleta, Spain. Observations were conducted during the Nov. 2008 bolometer pool. Zenith opacity for our observations was typically ∼0.2–0.3, and observations were carried out to a target 1σ sensitivity of 1 mJy, typically 20 min on source, in an ON-OFF pattern of 1 min on target followed by 1 minute on sky, with a throw of 32″. Flux calibration was carried out using Mars, and local pointing and secondary flux calibration were carried out using nearby bright quasars. The data were reduced using the facility reduction software MOPSIC[2]. We list the 1.2 mm continuum fluxes in Table B.2.

Table C.1. X-ray luminosities collected from the literature.

Star	log L_{Xray} (erg/s)	Instrument	Ref.
AB Aur	29.71	XMM	(1)
HD 31648	29.30	*Chandra*	(2)
HD 97048	29.58	XMM	(3)
HD 100453	28.82	*Chandra*	(4)
HD 100546	28.93	*Chandra*	(5)
HD 104237	30.11	*Chandra*	(5)
HD 135344 B	29.66	ROSAT	(6)
HD 141569A	<28.1	*Chandra*	(5)
HD 144668	28.3	*Chandra*	(7)
HD 150193	29.64	*Chandra*	(5)
51 Oph	<28.98	ROSAT	(8)
HD 163296	29.6	*Chandra*	(5)
HD 169142	29.1	*Chandra*	(9)
HR 4796 A	29.38	ROSAT	(10)

References. (1) Telleschi et al. (2007), (2) Grady et al. (2010), (3) Stelzer et al. (2004), (4) Collins et al. (2009), (5) Stelzer et al. (2006), (6) Grady et al. (2009), (7) Stelzer et al. (2009), (8) Berghoefer et al. (1996), (9) Grady et al. (2007), and (10) Stelzer & Neuhäuser (2000).

Table C.2. Continuum fluxes at 1.3 mm collected from the literature.

Star	$F_{1.3\ \mathrm{mm}}$ (mJy)	Error (mJy)	Instrument	Ref.
AB Aur	103	20	IRAM	(1)
HD 31648	360	20	OVRO	(2)
HD 36112	56	1	IRAM	(3)
CQ Tau	162	2	IRAM	(3)
HD 97048	450	30	IRAM	(1)
HD 100453	265	21	SIMBA/SEST	(4)
HD 100546	470	20	IRAM	(1)
HD 104237	90	20	IRAM	(1)
HD 135344B	142	19	UKT14/JCMT	(5)
HD 139614	242	15	UKT14/JCMT	(5)
HD 142527	1190	30	ATCA	(6)
HD 163296	780	30	OVRO	(2)
HD 169142	197	15	UKT14/JCMT	(5)
49 Cet	<2.1	–	SMA	(7)

References. (1) Henning et al. (1994), (2) Mannings et al. (1997), (3) Chapillon et al. (2008), (4) Meeus et al. (2002, 2003), (5) Sylvester et al. (1996), (6) Acke et al. (2004a), and (7) Hughes et al. (2008).

Appendix C: Data collected from the literature

In Tables C.1, C.2, C.3, and C.4, we list the X-ray luminosities, millimetre continuum fluxes, and CO line fluxes that we collected from the literature, as well as their references.

[2] http://www.iram.es/IRAMES/mainWiki/CookbookMopsic

Table C.3. ^{12}CO 2–1 line fluxes collected from the literature.

Star	^{12}CO 2–1 (Jy km s^{-1})	Error (Jy km s^{-1})	Instrument	Ref.
HD 31648	22.0	0.2	SMA	(1)
HD 36112	12.9	2.58	SMA	(2)
CQ Tau	3.10	0.18	SMA	(1)
HD 135344B	10.39	0.21	SMA	(1)
HD 139614	7.00	2.11	RxA3/JCMT	(3)
HD 142527	20.76	0.23	SMA	(1)
HD 142666	3.12	0.5	SMA	(22)
HD 163296	6.90	–	RxA3/JCMT	(3)
HD 169142	21.30	–	RxA3/JCMT	(3)
49 Ceti	2.0	0.3	SMA	(4)

References. (1) Öberg et al. (2010), (2) Isella et al. (2010), (3) Panic et al. (2009), and (4) Hughes et al. (2008).

Table C.4. ^{12}CO 3–2 line fluxes collected from the literature.

Star	^{12}CO 3–2 (Jy km s^{-1})	Error (Jy km s^{-1})	Instrument	Ref.
AB Aur	143.20[a]	3.29	RxB3/JCMT	(1)
HD 31648	53.00	1.16	RxB3/JCMT	(1)
HD 35187	<5.00	–	RxB3/JCMT	(1)
HD 36112	15.70	1.93	RxB3/JCMT	(1)
CQ Tau	6.00	0.97	RxB3/JCMT	(1)
HD 100546	178.4	19.20	APEX	(2)
HD 135344B	18.80	0.77	RxB3/JCMT	(1)
HD 139614	9.10	2.12	RxB3/JCMT	(1)
HD 141569A	14.70	1.16	RxB3/JCMT	(1)
HD 142666	13.90	2.70	RxB3/JCMT	(1)
HD 150193	1.40	–	RxB3/JCMT	(1)
HD 163296	8.30	1.93	RxB3/JCMT	(1)
HD 169142	32.9	2.51	RxB3/JCMT	(1)
49 Cet	6.58	1.35	RxB3/JCMT	(1)

Notes. [(a)] JCMT flux dominated by emission from the dark cloud.

References. (1) Dent et al. (2005) and (2) Panic et al. (2009).

References

Acke, B., & Waelkens, C. 2004, A&A, 427, 1009
Acke, B., van den Ancker, M. E., Dullemond, C. P., van Boekel, R., & Waters, L. B. F. M. 2004a, A&A, 422, 621
Acke, B., & van den Ancker, M. E. 2004b, A&A, 426, 151
Acke, B., van den Ancker, M. E., & Dullemond, C. P. 2005, A&A, 436, 209
Acke, B., Bouwman, J., Juhász, A., et al. 2010, ApJ, 718, 558
Alexander, R. D., Clarke, C. J., & Pringle, J. E. 2006, MNRAS, 369, 229
Alibert, Y., Mousis, O., Mordasini, Ch., & Benz, W. 2005, ApJ, 626, 57
Allende-Prieto, C., & Lambert, D. L. 1999, A&A, 352, 555
Andrews, S. M., Wilner, D. J., Espaillat, C., et al. 2011, ApJ, 732, 42
Aresu, G., Kamp, I., Meijerink, R., et al. 2011, A&A, 526, A163
Beckwith, S. V. W., Sargent, A., Chini, R. S., & Güsten, R. 1990, AJ, 99, 3
Benisty, M., Tatulli, E., Ménard, F., & Swain, M. R. 2010, A&A, 511, A75
Berghoefer, T. W., Schmitt, J. H. M. M., & Cassinelli, J. P. 1996, A&AS, 118, 481
Bitner, M. A., Richter, M. J., Lacy, J. H., et al. 2008, ApJ, 688, 1326
Bouwman, J., de Koter, A., Dominik, C., & Waters, L. B. F. M. 2003, A&A, 401, 577
Brandeker, A., Olofsson, G., Vandenbussche, B., et al. 2012, A&A, submitted
Brittain, S. D., Simon, Th., Najita, J. R., & Rettig, T. W. 2007, ApJ, 659, 685
Bross, I. D. J. 1971, Critical Levels, Statistical Language and Scientific Inference, in Foundations of Statistical Inference (Toronto: Holt, Rinehart & Winston of Canada, Ltd.), eds. V. P. Godambe, & D. A. Sprott
Brott, I., & Hauschildt, P. H. 2005, ESA SP-576, eds. C. Turon, K. S. O'Flaherty, & M. A. C. Perryman, 565
Bruderer, S., van Dishoeck, E. F., Doty, S. D., & Herczeg, G. J. 2012, A&A, 541, A91
Carmona, A. 2010, EM&P, 106, 71
Carmona, A., van den Ancker, M. E., & Henning, Th. 2007, A&A, 464, 687
Carmona, A., van den Ancker, M. E., Henning, Th., et al. 2008, A&A, 477, 839
Carmona, A., van der Plas, G., van den Ancker, M. E., et al. 2011, A&A, 533, A39
Cernicharo, J., Ceccarelli, C., Ménard, F., Pinte, C., & Fuente, A. 2009, ApJ, 703
Chapillon, E., Guilloteau, S., Dutrey, A., & Piétu, V. 2008, A&A, 488, 565
Chen, C. H., Li, A., Bohac, C., et al. 2007, ApJ, 666, 466
Collins, K. A., Grady, C. A., Hamaguchi, K., et al. 2009, ApJ, 697, 557
Corcoran, M., & Ray, T. P. 1998, A&A, 331, 146
Czechowski, A., & Mann, I. 2007, ApJ, 660, 1541
Dent, W. R. F., Greaves, J. S., & Coulson, I. M. 2005, MNRAS, 359, 663
Donehew, B., & Brittain, S. 2011, AJ, 141, 46
Dullemond, C. P., & Dominik, C. 2004, A&A, 421, 1075
Eiroa, C., Garzón, F., Alberdi, A., et al. (EXPORT) 2001, A&A, 365, 110
Fedele, D., Pascucci, I., Brittain, S., et al. 2011, ApJ, 732, 106
Feigelson, E. D., & Nelson, P. I. 1985, ApJ, 293, 192
Fumel, A., & Böhm, T. 2012, A&A, 540, A108
Goto, M., Usuda, T., Dullemond, C. P., et al. 2006, ApJ, 652, 758
Garcia Lopez, R., Natta, A., Testi L., & Habart, E. 2006, A&A, 459, 837
Gorti, U., & Hollenbach, D. 2009, ApJ, 690, 1539
Grady, C. A., Woodgate, B., Heap, S. R., et al. 2005, ApJ, 620, 470
Grady, C. A., Schneider, G., Hamaguchi, K., et al. 2007, ApJ, 665, 1391
Grady, C. A., Schneider, G., Sitko, M. L., et al. 2009, ApJ, 699, 1822
Grady, C. A., Hamaguchi, K., Schneider, G., et al. 2010, ApJ, 719, 1565
Gray, R. O., Corbally, C. J., Garrison, R. F., et al. 2006, AJ, 132, 161
Guimarães, M. M., Alencar, S. H. P., Corradi, W. J. B., & Vieira, S. L. A. 2006, A&A, 457, 581
Henning, Th., Launhardt, R., Steinacker, J., & Thamm, E. 1994, A&A, 291, 546
Herbig, G. H. 2005, AJ, 130, 815
Herbst, W., & Shevchenko, V. S. 1999, AJ, 118, 1043
Hillenbrand, L. A., Strom, S. E., Vrba, F. J., & Keene, J. 1992, ApJ, 397, 613
Ho, P. T. P., Moran, J. M., & Lo, K. Y. 2004, ApJ, 616, L1
Hollenbach, D., & McKee, C. F. 1989, ApJ, 342, 306
Hubrig, S., Stelzer, B., Schöller, M., et al. 2009, A&A, 502, 283
Hughes, A. M., Wilner, D. J., Kamp, I., & Hogerheijde, M. R. 2008, ApJ, 681, 626
Isella, A., Natta, A., Wilner, D., et al. 2010, ApJ, 725, 1735
Isobe, T., Feigelson, E. D., & Nelson, P. I. 1986, ApJ, 306, 490
Juhász, A., Bouwman, J., Henning, Th., et al. 2010, ApJ, 721, 431
Kamp, I, Tilling, I., Woitke, P., Thi, W.-F., & Hogerheijde, M. 2010, A&A, 510, A18
Kamp, I., Woitke, P., Pinte, C., et al. 2011, A&A, 532, A85
Kaufman, M. J., Wolfire, M. G., Hollenbach, D., & Luhman, M. L. 1999, ApJ, 527, 795
Keller, L. D., Sloan, G. C., Forrest, W. J., et al. 2008, ApJ, 684, 411
Koerner, D. W., Sargent, A. I., & Beckwith, S. V. W. 1993, Icarus, 106, 2
Kreysa, E., Gemuend, H.-P., Gromke, J., et al. 1998, SPIE Conf. Ser. 3357, ed. T. G. Phillips, 319
Lagrange, A.-M., Beust, H., Mouillet, D., et al. 1998, A&A, 330, 1091
Lavalley, M., Isobe, T., & Feigelson, E. 1992, Astronomical Data Analysis Software and Systems I, ASP Conf. Ser., 25, 245
Leinert, C., Richichi, A., & Haas, M. 1997, A&A, 318, 472
Levenhagen, R. S., & Leister, N. V. 2006, MNRAS, 371, 252
Liseau, R., Justtanont, K., & Tielens, A. G. G. M. 2006, A&A, 446, 561
Liskowsky, J. P., Brittain, S. D., Najita, J. R., et al. 2012, ApJ, submitted
Lorenzetti, D., Giannini, T., Nisini, B., et al. 20002, A&A, 395, 637
Mandell, A. M., Mumma, M. J., Blake, G. A., et al. 2008, ApJ, 681, L25
Mannings, V., & Sargent, A. I. 1997, ApJ, 490, 792
Manoj, P., Bhatt, H. C., Maheswar, G., & Muneer, S. 2006, ApJ, 653, 657
Martin-Zaïdi, C., Habart, E., Augereau, J.-C., et al. 2009, ApJ, 695, 1302
Martin-Zaïdi, C., Augereau, J.-C., Ménard, F., et al. 2010, A&A, 516, A110
Ercolana, B., Drake, J. J., Raymond, J. C., & Clarke, C. C. 2008, ApJ, 688, 398
Meeus, G., Waters, L. B. F. M., Bouwman, J., et al. 2001, A&A, 365, 476
Meeus, G., Bouwman, J., Dominik, C., et al. 2002, A&A, 392, 1039
Meeus, G., Bouwman, J., Dominik, C., et al. 2003, A&A, 402, 767
Meeus, G., Pinte, C., Woitke, P., et al. 2010, A&A, 518, L124
Mendigutía, I., Eiroa, C. Montesinos, B., et al. 2011a, A&A, 529, A34
Mendigutía, I., Calvet, N., Montesinos, B., et al. 2011b, A&A, 535, A99
Merín, B., Montesinos, B., Eiroa, C., et al. 2004, A&A, 419, 301
Montesinos, B., Eiroa, C., Mora, A., & Merín, B. 2009, A&A, 495, 901
Müller, A., van den Ancker, M. E., Launhardt, R., et al. 2011, A&A, 530, A85
Natta, A., Grinin, V., & Mannings, V. 2000, Protostars & Planets IV, 559
Oudmaijer, R. D., Palacios, J., Eiroa, C., et al. (EXPORT) 2001, A&A, 379, 564
Ott, S. 2010, in Astronomical Data Analysis Software and Systems XIX, eds. Y. Mizumoto, K.-I. Morita, & M. Ohishi, ASP Conf. Ser., 434, 139
Öberg, K. I., Qi, C., Fogel, J. K. J., et al. 2010, ApJ, 720, 480
Öberg, K. I., Qi, C., Fogel, J. K. J., et al. 2011, ApJ, 734, 98
Owen, J. E., Clarke, C. J., & Ercolano, B. 2012, MNRAS, 422, 1880
Panić, O., & Hogerheijde, M. R. 2009, A&A, 508, 707

Panić, O., Hogerheijde, M. R., Wilner, D., & Qi, C. 2008, A&A, 491, 219
Piétu, V., Dutrey, A., & Kahane, C. 2003, A&A, 398, 565
Pinte, C., Ménard, F., Duchêne, G., & Bastien, P. 2006, A&A, 459, 797
Pinte, C., Harries, T. J., Min, M., et al. 2009, A&A, 498, 967
Pinte, C., Woitke, P., Ménard, F., et al. 2010, A&A, 518, L126
Pilbratt, G. L., Riedinger, J. R., Passvogel, T., et al. 2010, A&A, 518, L1
Poglitsch, A., Waelkens, C., Geis, N., et al. 2010, A&A, 518, L2
Pollack, J. B., Hubickyj, O., Bodenheimer, P., et al. 1996, Icarus, 124, 62
Pontoppidan, K. M., Salyk, C., Blake, G. A., et al. 2010, ApJ, 720, 887
Riviere-Marichalar, P., Ménard, F., Thi, W. F., et al. 2012, A&A, 538, L3
Sandell, G. Weintraub, D. A., & Hamidouche, M. 2011, ApJ, 727, 26
Stelzer, B., & Neuhäuser, R. 2000, A&A, 361, 581
Stelzer, B., Micela, G., & Neuhäuser, R. 2004, A&A, 423, 1029
Stelzer, B., Micela, G., Hamaguchi, K., & Schmitt, J. H. M. M. 2006, A&A, 457, 223
Stelzer, B., Robrade, J. Schmitt, J. H. M. M., & Bouvier, J. 2008, A&A, 493, 1109
Sturm, B., Bouwman, J., Henning, Th., et al. 2010, A&A, 518, L129
Sylvester, R. J., Skinner, C. J., Barlow, M. J., et al. 1996, MNRAS, 279, 915
Tatulli, E., Benisty, M., Ménard, F., et al. 2011, A&A, 531, A1
Telleschi, A., Güdel, M., Briggs, K. R., et al. 2007, A&A, 468, 541
Testi, L., Natta, A., Shepherd, D. S., & Wilner, D. J. 2003, A&A, 403, 323
Thi, W.-F., & Bik, A. 2005, A&A, 438, 557
Thi, W.-F., van Dishoeck, E. F., Blake, G. A., et al. 2001, ApJ, 561, 1074
Thi, W.-F., Ménard, F., Meeus, G., et al. 2011, A&A, 530, L2
Tielens, A. G. G. M., & Hollenbach, D. 1985, ApJ, 291, 747
Tilling, I., Woitke, P., Meeus, G., et al. 2012, A&A, 538, A20
Torres, C. A. O., Quast, G. R., Da Silva, L., et al. 2006, A&A, 460, 695
van Boekel, R., Min, M., Waters, L. B. F. M., et al. 2005, A&A, 437, 189
van den Ancker, M. E., de Winter, D., & Tjin A Djie, H. R. E. 1998, A&A, 330, 145
van den Ancker, M. E., Meeus, G., Cami, J., Waters, L. B. F. M., & Waelkens, C. 2001, A&A, 369, 17
van der Plas, G., van den Ancker, M. E., Fedele, D., et al. 2008, A&A, 485, 487
van der Plas, G., van den Ancker, M. E., Acke, B., et al. 2009, A&A, 500, 1137
van der Plas, G., van den Ancker, M. E., Waters, L. B. F. M., & Dominik, C. 2012, A&A, submitted
van Leeuwen, F. 2007, A&A, 474, 653
Verhoeff, A. P., Min, M., Pantin, E., et al. 2011, A&A, 528, A91
Verhoeff, A., Waters, L. B. F. M., van den Ancker, M. E., et al. 2012, A&A, 538, A101
Woitke, P., Kamp, I., Thi, W.-F., et al. 2009a, A&A, 501, 383
Woitke, P., Thi, W. F., Kamp, I., & Hogerheijde, M. R. 2009b, A&A, 501, L5
Woitke, P., Pinte, C., Tilling, I., et al. 2010, MNRAS, 405, L26
Yang, H., Herczeg, G. J., Linsky, J. L., et al. 2012, ApJ, 744, 121
Yi, S., Demarque, P., Kim, Y.-Ch., et al. 2001, ApJS, 136, 417